Evaluation of rockfalls at a historical settlement area in the Ihlara valley (Cappadocia, Turkey) using different methods

Mehmet Sari (mehmetsari@aksaray.edu.tr)
Aksaray University https://orcid.org/0000-0001-9441-9256

Research Article

Keywords: Kinematical Analysis, Structurally Controlled Modes of Failure, Wedge Type and Block Toppling, 2D Rockfall Program

Posted Date: June 12th, 2021

DOI: https://doi.org/10.21203/rs.3.rs-242931/v1

Evaluation of rockfalls at a historical settlement area in the Ihlara valley (Cappadocia, Turkey) using different methods

Abstract

Rockfalls are one of the most dangerous natural events in hilly terrains. This study presents the results of an investigation program to analyze the possibility of a rockfall from a slope to nearby residential buildings in a historical settlement area. Various rockfall analysis techniques were implemented in the study for this purpose. The kinematical analysis revealed the potential of different structurally controlled modes of failure in the slope, especially wedge type and block toppling were the most significant ones. Finite element analysis suggested a stable slope considering the safety factor of 2.19 for the existing geological and geotechnical conditions of the studied slope case. A possible rockfall trajectory was determined and located as an input in the 2D rockfall program based on the field measurements. Different shapes and sizes of blocks were used in the rigid body model for a more realistic numerical simulation of rockfall events. According to the 2D model results, there was no danger of rockfall for the investigated downslope buildings. However, to stay on a safe side, a suitable control measure with a specified dimension was proposed to manage rockfalls in the study area.

1. Introduction

Rockfalls are among the most dangerous natural events in mountainous terrains, road cuts, quarry faces, and coastal cliffs (Spadari et al. 2012). Rockfall is defined as "the free-falling or precipitous movement of newly detached segments of the bedrock of any size from a cliff or other very steep slope" (UN Glossary 2020). They occur when a rock fragment, isolated rock, or boulder is detached from a steep rock wall, cliff, or slope and then travels some distance by free-falling, bouncing, rolling, and sliding (Fig. 1-a). Since they occur suddenly, it is not possible to forecast rock falls in advance. Therefore, they pose a severe threat to humans, buildings, and groundworks, particularly if they are not accurately documented for the risk they source (Fig. 1-b). It is necessary to assess the danger induced by rockfall to secure endangered human lives, residential areas, and infrastructure in closer vicinity (Dorren 2003). Favorable geology and climate are the main factors controlling rockfall occurrence. They include intact behavior of the bedrock, fractures in the rock mass, exposure

to weathering, presence of water, freezing-thawing processes, root-wedging, and exterior forces (Attewell and Farmer 1976; Bozollo and Pamini 1986; Giani 1992; Dorren et al. 2006; Binal and Ercanoğlu 2010; Asteriou et al. 2012). Some biological, mechanical, and environmental actions (i.e., seismic activity, ground vibrations, pore-water pressure changes due to heavy rainfall, erosion of surrounding soil during heavy storms, root-growth, or leverage by roots moving in strong winds) can also trigger rockfalls (Hoek 2007).

In this study, an investigation program was undertaken to figure out rock falls to houses in a historical settlement area due to a nearby rock slope (Fig. 2). The study area includes the historical Belisirma village (Guzelyurt-Aksaray), which belongs to a special protection area covering 14 km length Ihlara valley and its surroundings. The site has only been studied in terms of geotechnical and rock mechanics perspectives by a few researchers. Binal (1996) investigated the instability mechanisms observed in volcano-sedimentary rocks, especially in the Kizilkaya ignimbrite in the valley. According to the kinematic analysis results, the study found that the toppling failure was the most probable mechanism in a single block with an eroded base and the system of several blocks in the Kizilkaya ignimbrites. The secondary toppling occurs when an individual block's base angle exceeds 8^{o} and should exceed 11^{o} due to differential settlement in the block groups. Sarı and Çömlekçiler (2007) characterized the Kizilkaya ignimbrite using the rock mass rating (RMR) (Bieniawski 1989) classification system. They described the rock mass as "good" with a total score of 62.

Tunusluoglu and Zorlu (2009) investigated the rockfall hazard at one of the natural and historical monuments in the Cappadocia region. In the fieldwork, they described the location and dimension of the moved-in-place blocks having the potential to fall. After determining the necessary input parameters, they analyzed the threat caused by these blocks using rockfall software. A potential risk map showing the areas under rockfall danger around the castle was prepared in the study. Sari (2009) developed a stochastic model to estimate the Kizilkaya ignimbrite properties using the Monte Carlo simulation method. He defined the best-fitting frequency distributions for each input parameter of the generalized Hoek-Brown criterion during the simulation process. He found that the strength and deformability parameters of the Kizilkaya ignimbrite could be approximated by asymptotic distributions skewing to larger values like intact rocks. Zorlu et al. (2011) considered the effect of the landforms on the rockfall hazard assessment in the Cappadocia region. They found that differences in the durability between the horizontal layers of the slope were the significant

causes of severe rockfall events. In the region, the uppermost levels were composed of well-cemented limestones and welded ignimbrites, whereas the lower parts and slopes were composed of soft tuffs and non-welded ignimbrites. Taşpınar (2015) developed various two-dimensional (2D) computer models to assess rockfall hazards in the different parts of the Ihlara valley. She found that it was likely to observe different falling scenarios depending on the block sizes in the Kizilkaya ignimbrite. Ozturk et al. (2019) proposed a low-cost and useful approach for determining orientation (strike and dip) of fractures in a computerized environment using mobile phones and photogrammetric methods. They applied the proposed methodology to a part of the Ihlara valley where the rock units' columnar structure did not allow the discontinuity measurements with a conventional surveying method. A recent numerical study by Sari (2021) in a different part of the Ihlara valley has shown that the valley's cliffs were highly susceptible to secondary toppling failure. In this process, the soft basal rock has been eroded due to water and wind erosion over time (i.e., undercutting), while the block falls from above the hard ignimbritic rock were observed as a result of differential settlement and deformation at the base. Nearly vertical orthogonal joint sets in the upper blocky rock mass have a primary role in promoting the valley's rockfall activity.

It is possible to observe different failure mechanisms in a rock slope with the same geological features depending on the joints' geometric properties and the slope face. To better reflect actual rockfall behavior, it requires a careful characterization of parameters in the field for numerical modeling. Firstly, discontinuity measurements were performed on the rock mass source leading to rockfall on the northeast of the buildings. Different structurally controlled failure modes were investigated for the kinematical analysis depending on the orientation of slope and friction angle of the discontinuities. Secondly, the minimum safety factor was searched under the geological and geotechnical conditions of the slope using the finite element method (FEM). Lastly, different shapes and sizes of blocks, possibly fallen from the slope due to weak structural planes, were simulated using a two-dimensional (2D) rockfall analysis program. Maximum runout distances, bounce height, and total kinetic energy of the rock blocks were determined along the assumed trajectory. Based on the rockfall danger zone defined by the 2D model, a retention wall with a specified location and size was implemented to secure the houses in the study area.

2. Study Area

The historical Belisırma village belonging to Guzelyurt town is located 35 km southeast of Aksaray city. This village is part of the touristic Ihlara valley, which is well-known due to its historical and cultural heritage and natural beauty. The length of the valley is 14 km with a 52 km^2 area (Şimşek 1997). Hasan-Melendiz mountain range, which lies along the E-W direction and the highest altitude belongs to Hasandağ (3257 m), is bordered by flat-lying plains with an average altitude of between 1100 and 1400 m. The most significant relief structure in the region is the drainage system of the Melendiz river on the north flank of the Hasandağ (Doğan et al. 2019). This system cuts thick ignimbrite-intercalated fluvio-lacustrine sediments. As a result, canyon-like deep valleys were generally formed in the region. The study area's stratigraphy is mainly composed of late Miocene-Quaternary age young volcano-sedimentary units, including the pyroclastic rocks of Hasandagi ashes, Selime tuff, and Kizilkaya ignimbrite.

2.1. Hasandağı Ashes (Th)

Hadandağı ashes were formed by the sequential deposition of lacustrine sediments and volcanic products in the area. Rock types in this formation showed vertical and horizontal transitions. It has a flat topography with a gentle slope. Since it filled the previous surface topography, Hasandağı ashes offer highly variable thicknesses in the region. In general, this formation consists of grayish-white ashes and lapilli in which the white-colored vitric ash matrix includes obsidian, pumice, and lava fragments in sizes from coarse-grained sand to 5-6 cm in diameter. Hasandağı ashes cover the Kizilkaya ignimbrite on the west flanks of the Ihlara valley.

2.2. Selime Tuff (Ts)

Selime tuff, which covers a considerable part of the study area with its light purple to yellowish-white color, was first named after Beekman (1966). It lies in a narrower band along the valley starting from the Ihlara town and outcrops on a broader domain around the Selime town. Selime tuff is recognized with Neogene-aged fairy chimneys, a spectacular badland landscape for Turkey's Cappadocia region. Fairy chimneys are specific landforms that originated from differential eroding of pyroclastic-flow deposits consisting of a very poorly sorted mixture of volcanic ash or tuff during pumice lithification with rock fragments

in fluvio-lacustrine environments (Sarikaya et al. 2015). When it was eroded together with overlying hard Kizilkaya ignimbrite, an impressive mesa capping a badland landscape on the valley's right bank was observed in the region. Selime tuff is rich in basalt, spilite, obsidian, tuffite, pumice, and andesite fragments showing locally color change facies in a light purple to whitish-yellow. In these facies, the radius of the pumice fragments also increases in the tuff.

2.3. Kizilkaya Ignimbrite (Tk)

The welded Kizilkaya ignimbrite outcropping of various sizes in the region has the widest distribution, which is mesa hills with a badland landscape. The most beautiful location in which the contact relationship of this mesa unit and the Selime tuff underneath is seen in the north of Kızılkaya village. Beekman (1966) named ignimbrites as Kızılkaya ignimbrite about this area. It is generally whitish-gray, with slightly weathered surfaces turning a pinkish color. The ignimbrite, which has a flat-looking topography, was divided into pieces by the Melendiz river and its tributaries forming mesa hills at various heights. In the Ihlara valley, which is in the form of a deep narrow canyon, Kizilkaya ignimbrite shows pervasive columnar jointing due to cracks developed in sub-vertical direction during the cooling. The thickness of ignimbrite reaches approximately 60 m in the valley. It contains pumice fragments with weakly textured at the upper levels, densely textured at the middle classes, and rough, densely textured at the bottom up to 30 cm in size. A red-colored cooking zone is noticed between Kizilkaya ignimbrite and the underlying Selime tuff. The thickness of the Kizilkaya unit varies between 2-75 m in the study area. Kızılkaya ignimbrite's age was 4.9-5.5 million years found by the K/Ar method in biotites (Ayhan and Papak 1988).

3. Rockfall Analysis Using Different Methods

3.1. Kinematical analysis

The kinematical analysis is a practical preliminary method to investigate the stability of rock slopes in which the failure is mostly controlled by the predominant discontinuity sets in the rock mass (Hoek and Bray 1991). According to the structural and engineering geology studies related to the field, discontinuity systems can create kinematically different rock mass instabilities in the studied slope. For initiating a rockfall, a block should be formed by two intersecting joints, and it is kinematically capable of dislodging from the slope face. In

this process, kinematical analysis is the first step in identifying slope conditions for potential structurally controlled failures, such as plane, wedge, and toppling (Hoek and Bray 1991). Therefore, before doing any rockfall analysis, it is crucial to recognize structural discontinuities with respect to the orientation of the slope face. Fig. 4 shows the typical failure modes and conditions for the kinematic analysis. These may take the form of a plane failure (Fig. 4-a) in which rock mass contains continuous joints dipping out of the slope face, and they strike parallel to the slope face; a wedge failure (Fig. 4-b) formed by two intersecting planes of discontinuities; toppling failure (Fig. 4-c) in which rock mass contains fractures steeply dipping into the face; and a circular failure (Fig. 4-d) in the rock fill, very weak/weathered rock or closely jointed rock masses containing many randomly oriented discontinuities (Wyllie and Mah 2004).

Given that discontinuities play a critical role in the kinematical analysis, 53 discontinuity measurements were performed on the hard ignimbritic unit covering the slope (Fig. 5-a). Two sub-vertical orthogonal joint sets were delineated from the rock mass forming the slope crest. A third joint set lying horizontally is almost perpendicular to these two sets (Fig. 6). Sub-vertical joint sets (Set 1 and Set 2) were developed as a result of thermal cracks formed while the cooling of ignimbrite massif took place. Near horizontal joint set (Set 3) was formed from different outflow facies during ignimbritic deposition (Sarı and Çömlekçiler 2007). Table 1 presents some characteristics of the discontinuity sets in the rock mass and other input parameters necessary for the kinematic analysis. Tilting tests were conducted in the field to estimate the friction angle of the discontinuity surfaces (Fig. 5-a). This test is based on measuring the friction angle between two blocks placed on top of each other in the field directly when the upper one starts to slide on the lower one. It is an in-situ test for better reflecting the actual conditions in the field and considering the size effect. The average of three tilting tests was calculated as ϕ=45^{o}.

The rock mass lies on the upper slope of the houses subjected to rockfall (see Fig. 2-a). The analysis considers the SW face of the slope looking towards the houses (Fig. 2-b). Accordingly, the slope's dip/dip direction was recorded as 85^{o}/205^{o} in the field. For the rock mass in the slope, three joint sets had been identified with a dip/dip direction of joint set 1 (86^{o}/275^{o}), joint set 2 (88^{o}/194^{o}), and bedding set 3 (2^{o}/201^{o}). Goodman (1989) and Hoek and Bray (1991) described the method employed in kinematic analysis using the lower

hemisphere stereonet projection. The data in Table 1 was used in Dips v.8.0 software (Rocscience Inc. 2020a) for analyzing modes of the planar, wedge, and toppling failures.

3.2.1. Planar Failure

Compared to other modes of failure, planar failure usually occurs seldom in nature. In the kinematic analysis of a planar instability, the critical zone is defined as the area encircled by the outside of the pole friction cone and inside the daylight envelope. The poles located within this zone are likely to slide. Accordingly, the slip plane angle must be greater than the friction angle and smaller than the slope's inclination. Also, the direction of the slip plane and the slope must be approximately parallel to each other. In other words, the difference between the dip direction of the slip plane and the slope should be at most ±20° (Goodman 1989). Fig. 7 presents suitable conditions for a planar sliding on the stereonet. Each discontinuity that falls into the red shaded region has a planar sliding potential. Accordingly, out of 53 discontinuity surfaces measured in the field, only 3 of them are located in the critical region, and these three discontinuity planes are members of Set 2. As a result, the potential for planar sliding on this slope has been calculated as 5.66 %.

3.2.2. Wedge Failure

In case two intersecting planes form a rock wedge, and if it slides along the intersection direction, it is called a wedge failure. In the stereonet, the area inside the friction cone plane and outside the slope's plane is the critical zone. Wedge instability is characterized by the joint planes intersected in the critical zone (Wyllie and Mah 2004). The stereoplot program calculates the trend and the plunge of all intersecting planes. At least two different pole concentrations must be observed on the stereonet for a wedge-type sliding. The red shaded region given in Fig. 8 is considered as the critical zone. The intersections falling in this region have the potential of wedge-type failure. Accordingly, out of the 1377 intersections formed by the three sets on the slope, only 229 were plotted in the critical zone. As a result, the potential for wedge-type failure on this slope was found to be 16.63%.

3.2.3. Toppling Failure

Toppling is a common failure type in slopes with sub-vertical joints. In this failure type, rock columns or blocks have to rotate along a fixed base. Toppling instability is classified broadly

as direct or block toppling and flexural toppling. In block toppling, rock columns are formed by one set of joints steeply dipping into the slope face, and the length of broadly spaced cross joints defines the column height. However, in flexural toppling, the rock columns separated by the continuous joints can bend forward before instability (Wyllie and Mah 2004). The slip limit plane in the steorenet plot defines the critical zone in flexural toppling. The deduction of friction angle from the slope angle gives the dip of the slip limit plane, and its dip direction is the same as the dip direction of the slope face. The other condition for toppling is that the difference between the slope's dip direction and the discontinuity sets needs to be within ±30° (Goodman 1989). The pole plots within the critical zone in Fig. 9 illustrate the block toppling. Accordingly, the block failure was observed in only 112 of 1377 intersections defined on the studied slope. That is, the direct block failure potential on this slope was found to be 8.13%. The potential for oblique (lateral) block failure on this slope was calculated as 10.9%. One of the most critical factors controlling block toppling was the presence of a basal plane on which the blocks would topple. The majority of the discontinuities (58.82%) in Set 3 form the basal plane where the slip would occur. When the flexural type of toppling failure was considered in Fig. 10, only four discontinuity planes showed a potential for this type of failure with a percentage of 7.55 among the evaluated discontinuities.

The kinematic analysis results given in Table 2 indicated that wedge and toppling failures would be the leading cause of block instability in the slope. As shown in Fig. 11, some of the wedges observed on the downslope show consistency with the kinematic analysis results.

3.3. Shear Strength of Discontinuities

The rock mass is a geologic structure divided by visible defects into intact rock blocks of various sizes. In engineering excavation built in/on rock structures very close to the surface, where the effective stresses are very low, the failure and deformation are mainly governed by the shearing resistance of the discontinuity surfaces (Barton and Choubey 1977). In planar discontinuity surfaces, since there was not enough resisting force against the shearing, it could damage the geologic structure with a minimum stress change. Filling materials like clay, silt, calcite can be easily worn out, and the discontinuity surface is now in the state of residual shear strength (Barton et al. 1974). On the other hand, roughness and undulation have more pronounced effects on the shear strength of natural joint planes. In general, the

shear strength of rock joints increases as the surface roughness increases, and it is essential for the stability of rock excavation (Barton 1973). In this study, the non-linear Barton-Bandis (BB) shear failure criterion (Barton et al. 1974; Barton and Choubey 1977) is used to determine the shear strength of rock joints due to its simplicity and easiness. Barton et al. (1974) had studied the natural joint planes and proposed the following equation:

$$\tau_p = \sigma_n \tan\left[\phi_b + JRC \log_{10}\left(\frac{JCS}{\sigma_n}\right)\right] \quad (1)$$

where τ_p and σ_n are the shear and normal stresses, respectively; JRC is the joint roughness coefficient; JCS is the joint wall compressive strength; and ϕ_b is the basic friction angle of the unweathered rock surface.

Later, Barton and Choubey (1977) changed this formula by using 130 direct shear box experimental results of joint surfaces in weathered rocks.

$$\tau_p = \sigma_n \tan\left[\phi_r + JRC \log_{10}\left(\frac{JCS}{\sigma_n}\right)\right] \quad (2)$$

Where ϕ_r is the residual friction angle, Barton and Choubey (1977) determined that the friction angle can now be estimated as:

$$\phi_r = (\phi_b - 20) + 20\left(\frac{r}{R}\right) \quad (3)$$

Here, r is the Schmidt value of the wet and weathered surface, R is the Schmidt value of the non-weathered fresh surface. It can be seen that the basic friction angle (ϕ_b) plays a crucial role in predicting the shear strength of the discontinuities. The basic friction angle characterizes fresh surfaces. The basic friction angle has been investigated by Barton and Choubey (1977) for different rock types, and they recommended 25°-30° for sedimentary rocks, and 30°-35 ° for magmatic and metamorphic rocks. The basic friction angle can be calculated for fresh, smooth surfaces using the tilt test or the direct shear box test in the laboratory (Alejano et al., 2012).

The joint roughness coefficient (JRC) was extracted from the joint surfaces of hard ignimbrite in the slope crest. As seen in Fig. 12-a, a wooden ruler 1 m in length was placed on the joint surface to measure asperity amplitude using a vernier caliper. The average asperity amplitude value (a=22.2 mm) measured on the discontinuity surfaces was located

on the graph in Fig. 13 to find a JRC value of 10. The joint wall compressive strength (JCS) was obtained from the Schmidt hammer test. This test is a practical indirect method for predicting the compressive strength of joint planes in the field. The hammer was applied perpendicular to the discontinuity surfaces during the test. Accordingly, the JCS value of joint surfaces in ignimbrite rock was found using the graph in Fig. 14, which was developed by Barton and Choubey (1977) from the equation proposed by Deere and Miller (1966). The JCS value was found to 55 MPa for the unit weight γ_d=21.95 kN/m^3 and Schmidt hardness value, r=38.2, measured on the weathered joint surfaces in the field.

In this study, the basic friction angle was obtained by performing a simple tilt test where a manually-operated wooden table was utilized in the experiments. The most widely used method for this test was early proposed by Stimpson (1981), and later this method was revised by Alejano et al. (2012). As shown in Fig. 15, two disc-shaped specimens prepared for the Brazilian tensile test were used in the experiments, which had more conservative values than other sample shapes. Eq. (4) was used for the conversion of β to the basic friction angle.

$$\phi_b = \tan^{-1}\left(\frac{2}{\sqrt{3}}\tan\beta\right) \tag{4}$$

Here β is the slope of the tilt assembly at the start time of the slide.

The residual friction angle was calculated according to Eq. (3) using the basic friction angle obtained from the tilt test. Accordingly, the peak friction angle for discontinuity planes of hard ignimbrite was determined as ϕ_p=52.6 degrees. The BB failure envelope of the joints based on Eq. (2) is depicted in Fig. 16. Using the least-square regression technique, the non-linear BB failure envelope was then linearized in the range of normal stresses effective in the rock mass to implement Mohr-Coulomb's linear model for the numerical analysis in the next section.

3.2. Finite Element Analysis

The stability of the slopes is one of the most studied and widespread geotechnical analyses in engineering problems. It is essential to understand the processes and mechanism driving the instability in an unstable rock slope to evaluate the potential hazard associated with it

(Eberhardt et al. 2002). There are several numerical methods used in solving such instability problems. The finite element method (FEM) is a numerical method mostly utilized in the failure behavior of continuous rock masses under effective in-situ stress conditions. Due to the capabilities of FEM, many studies in recent years were conducted using this method in the modeling of rock mechanics related problems (Hammah et al. 2007; 2008; 2009; Fu and Liao 2010; Azami et al. 2012; Pain et al. 2014; Alemdag et al. 2019; Sari 2019). Due to the simplicity of its coding programs, less computation power and time, this method was employed to perform the numerical analysis in this study. This method can analyze the rock mass's failure propagation within defined structural defects such as joints, faults, fissures, schistosity, foliation, folding, and beddings.

It is a well-known fact that the stability of rock slopes is significantly affected by discontinuities in the rock mass since the discontinuities control the rock mass's overall structure and mechanical properties (Hoek et al. 2002). The joint intersections are the potential locations of high stress, deformation counters, shear damage, and instability (Mas Ivars, 2010). Besides, the effect of external forces such as groundwater and earthquake loads can be easily incorporated into built FEM models. It is also probable to define different rock material and rock mass constitutive models for the materials forming the slope. At the end of the analysis, a unique safety factor representing the slope's stability condition can be calculated numerically using the shear strength reduction (SSR) method (Sari 2019). A critical strength reduction factor (SRF) can be easily predicted with total displacement and major shear strain counters of the failed slope. Using this method, the possible location of the unstable rock blocks can be defined.

A reliable slope stability analysis needs to assume the right failure criteria with accurate input parameters in jointed rock masses (Sari 2019). An experimental study was undertaken to obtain the unit weight, uniaxial compressive strength (UCS), Brazilian tensile strength (BTS), and Schmidt hardness value of rock materials based on ISRM (2007). UCS and BTS tests were conducted using NX (diameter 54.00 mm) core sizes (Fig. 17). It was unlikely to have high-quality standard core specimens from the coarse-grained tuff blocks since they were exposed to intense weathering. The test results were imported into RocData v.5.0 software (Rocscience Inc. 2020b). The best-fitting generalized Hoek-Brown (HB) failure criterion envelopes are shown in Fig. 18 and Fig. 19 for the intact rock samples. Hoek et al. (2002) developed the HB failure criterion for upscaling the strength envelopes obtained from

the rock material to the field scale rock masses. HB failure criterion provides a dimensionless equation given in Eq. (5) to connect geological observations with calculations.

$$\sigma_1 = \sigma_3 + \sigma_{ci}\left(m_b \frac{\sigma_3}{\sigma_{ci}} + s\right)^a \quad (5)$$

Here, σ_1 and σ_3 are the major and minor principal stresses, respectively. To estimate the jointed rock mass's strength in a confined state, four parameters are needed: the unconfined compressive strength of the intact rock, σ_{ci}, and HB constants m_b, s, and a. The geological strength index (GSI), the disturbance factor, D, and the intact rock material constant, m_i, can be employed to obtain the parameters using the following equations (Hoek et al. 2002):

$$m_b = m_i exp\left(\frac{GSI-100}{28-14D}\right) \quad (6)$$

$$s = exp\left(\frac{GSI-100}{9-3D}\right) \quad (7)$$

$$a = \frac{1}{2} + \frac{1}{6}\left(exp\left(\frac{-GSI}{15}\right) - exp\left(\frac{-20}{3}\right)\right) \quad (8)$$

GSI plays a critical role in the HB failure criterion, and a visual chart is provided for a qualitative description of the rock mass structural elements and discontinuity surface conditions. The GSI values of the studied rock masses were directly determined in the field following the GSI chart provided by Marinos and Hoek (2000), as seen in Fig. 20. According to the field observations, the slope's rock structure had been separated into two distinct zones. The upper welded zone was named "hard ignimbrite" while the lower unwelded zone bearing rock carved structures was named "soft ignimbrite". The rock formation covering the downslope surface between the slope and the dwellings was called "tuff". The strength envelopes of three rock masses showed significant variations as presented in Fig. 21, both for principal and shear-normal stress spaces. The resulting rock mass properties in Table 3 were employed in the 2D finite element analysis program RS2 v.2019 (Rocscience Inc. 2020c).

The FEM model used in numerical analysis is shown in Fig. 22, with necessary assumptions applied during the model building stage. Vertical and horizontal in-situ stresses are assumed to be equal. The bottom, left, and right nodes of the model are fixed, and the top surface of the model is free in all directions. Sub-vertical and horizontally oriented discontinuities are explicitly defined as infinite parallel joint sets (Set 2 and Set 3) within the hard ignimbrite

mass forming the top of the slope. Two caves representing the rock-carved structures built for sheltering or worshiping by the ancient people living in the region are added to the soft ignimbrite closer to the slope's toe. The dimensions of the slope and caves are comparable with the actual values measured in the field.

The outputs of the maximum shear strain and total displacement counters of the FEM model are presented in Figs. 23 and 24, respectively. If the maximum shear strains were considered on the slope in Fig. 23, the leading factor for the slope failure would be due to the collapse of the old dwellings excavated inside the soft ignimbrite. The presence of artificial caves and dwellings is one of the main factors promoting instability in the rock masses in the Ihlara valley (Sari 2021). The weight of the above hard ignimbrite would cause continuous damage on the boundary of caves over time. The FEM analysis results agreed with the actual field observations as seen in the exaggerated inset picture. Furthermore, a relatively high value of SRF= 2.19 was found by the SSR analysis. This value indicates that the overall slope failure would occur in a long period. For an immediate collapse, the calculated SRF value should be 1.0 or below. In the case of the total displacement counters on the slope face that were considered in Fig. 24, one can easily discern that the major movements would take place on the slope crest where the hard ignimbrite was separated into many intersecting blocks by discontunity planes. It clearly shows unstable blocks on the studied slope as a source area of potential rockfalls.

3.3. Rockfall Analysis

Rockfall analysis is a function of the source area's location, the geometry, and geomechanical properties of both the block and the slope. In theory, if the initial conditions, the slope geometry, and the energy loss at impact or by rolling can be determined initially, it is probable to measure the position and velocity of a block at any time. In practice, however, it is often impossible to accurately determine the exact location of source points of the rock blocks and their size, shape, and geomechanical properties. Besides, the surface formation's geometrical and mechanical properties can change considerably along a slope (Agliardi and Crosta 2003). Slope geometry, slope roughness, static and dynamic friction, rolling resistance, the density of rocks, and the restitution coefficients are the most important parameters defining particular rockfall trajectories. Among these physical properties, the coefficient of restitution plays a significant role in locating the exact rockfall trajectory

(Ansari et al., 2015). It is also the most important input parameter quantifying the energy absorption upon an impact (Ji et al., 2019). It depends on the rock type covering the surface, the vegetation cover, the shape and size of the falling block, and the slope's physical properties (Dorren et al., 2006; Dadashzade et al., 2014). Therefore, a reliable estimation of the coefficient of restitution is of profound importance in rockfall prediction and for designing countermeasures against rockfall (Chau et al. 2002).

In the lumped-mass impact models, the normal and tangential coefficients of restitution (R_n and R_t, respectively) are employed to replace the lack of physics required by the basic equations. The normal coefficient of restitution, R_n, is the amount of energy loss during a falling body's impact in the slope's normal direction. The tangential coefficient of restitution, R_t, is the amount of resisting forces caused due to moving parallel to the slope. Site-specific restitution coefficients can be estimated directly from laboratory or field tests, back analysis of falling blocks, or using theoretical estimation methods (Bozzolo and Pamini 1986; Kobayashi et al. 1990; Evans and Hungr 1993; Budetta and Santo 1994; Robotham et al. 1995; Chau et al. 2002). The most common method is to estimate them from the back analysis of measured rock paths and end locations during the field tests of rockfall trajectory (Bar et al. 2016).

In this study, the coefficients of restitution were determined from a back analysis in RocFall v.5.0 software (Rocscience Inc. 2020d). For this purpose, the location and size of the two fallen blocks observed in the study area were measured during field visits. As seen in Fig. 25, one of the blocks was 10 m away from the slope toe, and the second one was 8 m away. By considering the weights of the blocks and their distances from the slope toe, the corresponding normal (R_n) and tangent (R_t) restitution coefficients of tuff forming the downslope surface were determined R_n=0.25 and R_t= 0.60 according to back analysis results given in Fig. 26. In this process, the required parameters were adjusted incrementally until modeled runout paths showed a similar spatial distribution to the actual block locations.

For the houses located at downslope, two dimensional (2D) rockfall analysis was executed along the AA-section line on the slope using RocFall v.5.0 software (Fig. 27). The program simulates the rockfall trajectory of the potentially unstable rock blocks by calculating runout distance, bounce height, and total kinetic energy for the given 2D profile. RocFall program additionally allows the user to perform both lumped-mass and rigid body rockfall analysis

methods. In the lumped-mass models, a block is considered as a tiny particle with a mass. Falling rock is defined as a point mass; the actual size and shape are neglected even though they would otherwise affect its trajectory (Rocscience Inc. 2020d). In lumped-mass impact models, the mass of fall rock is only used to calculate energies, and it does not affect the overall body trajectory. Only the sliding motion is replicated while the rotation is characterized by a zero friction angle (Basson 2012). On the other hand, in rigid-body impact models, the essence of fall rock behavior is captured by using the laws of motion and kinematics. It is assumed an instant contact period and that the contact area between the impacting objects is insignificant. The fallen rock's shape and size with four types of movement (i.e., fall, slide, bounce, and roll) are considered in rigid-body impact models (Basson 2012). Modeling all four modes of motion is necessary for a realistic, more consistent risk-based rockfall hazard study (Vick et al., 2019).

In this study, the rigid body impact module is used in the rockfall analysis to obtain more realistic outcomes. Discrete rockfall boulders are modeled with arbitrary and random shapes and size/mass. Various smooth and polygon shapes of sphere, square, triangle, egg, oval, ellipse, rhombus, rectangle, pentagon, hexagon, and octagon were specified for the potentially unstable blocks. The size/mass of a block had been selected based on the varying in-situ block sizes and the average density of hard ignimbrite. The densities of the ignimbrite blocks were determined on the core samples in the laboratory. Accordingly, the dry density of ignimbrites was measured as 2.17 gr/cm^3, and the water-saturated density was 2.24 gr/cm^3. In rockfall analysis, generally, considering the worst condition, water-saturated density is more applicable in determining the block weights. Thus, the varying block sizes of 10 kg, 100 kg, 1,000 kg, 5,000 kg, 10,000 kg, and 20,000 kg were executed in rockfall analysis. A total of 1,200 simulations were realized using the blocks in different shapes and sizes to cover possible rockfall trajectory scenarios. Due to the slope geometry and block orientation restrictions, initial velocities of the blocks in vertical and horizontal directions were taken to be 0.5 m/s in the model. Other input parameters selected in the analysis are given in Table 4. With difficulty in data availability, some of these input parameters were estimated from the typical values used in the RocFall program's case histories.

The rockfall analysis results for the AA-section profile are presented in Fig. 28 and Table 5. According to the results of the 2D analysis, blocks falling from the crest of 18 m high rock

slope reached a maximum runout distance of 21.13 m. Most of the blocks were stopped after bouncing and rolling at a small distance from the slope toe. It appears that none of the blocks modeled by the program can reach the houses located at a distance of approximately 55 m (see Fig. 28). In terms of movement mechanism, a block that can detach from the upper elevations of the steep slope primarily exhibits a free-fall at the beginning. Later, the block hits and bounces on the horizontal surface near the slope toe. After very low bouncing heights (60-75 cm), the block rolls down along the slope surface, loses its kinetic energy, and stops when it reaches the flat area. The observations made in the field also confirmed the simulated paths. Previously fallen rock blocks in various sizes were also very close to simulated locations in the model.

The number of blocks and their runout distances, the bouncing heights, and total kinetic energies on the slope profile was also determined during the rockfall analysis. To design a practical mitigation structure, the endangered rockfall zone and the impact energy of falling rocks must be accurately predicted (Yan et al. 2020). Accordingly, most of the blocks were rolled not more than 10 m horizontal distance on the slope profile. Out of 1,200 simulated rock boulders, only twelve could reach up to 20 m distance (Fig. 29). When the bouncing heights given in Fig. 30 were evaluated, it was seen that the blocks jumped up to 8 m mean bounce height at first impact, but as they move away from the slope toe, their bounce heights decrease suddenly. It was found that the block that could travel the farthest distance would jump only 1.1 m. When the total kinetic energy distribution given in Fig. 31 was examined, similarly, the blocks had mean kinetic energy (244 kJ) with the effect of the free fall at the beginning, but they lose this energy as a result of friction during the rolling along the lower section of the slope, and this value decreases up to 12 kJ at rest.

3.4. Mitigation Against Rockfalls

For the planning of rockfall mitigation measures such as protective barriers, it is necessary to determine the maximum kinetic energies (for the bearing capacity of the protective barrier to hold the rock block) and the largest jump heights (for the barrier height) of the potential rock blocks. Also, the evaluation of the runout distance for estimating the rockfall hazard zone is another necessity. The 2D rockfall analysis showed that ignimbrite blocks of different sizes and shapes detached from the steep slope with a height of about 18 m could not reach the dwellings subject to investigation. However, there is always a risk of falling

rocks for dwellings in the study area, and necessary precautions should be taken to mitigate this danger.

Typically, rockfall events can be mitigated either by active or passive measures. In passive mitigation, the rockfall can still occur, but an effort should be made to prevent the consequence. The negative effects of rockfall events can be diminished by employing rockfall catchment fences, drape nets, diversion dams, rock sheds, and forest belts in the runout or deposition zones. However, in the active mitigation, rockfall event occurrence is prevented from the source zone by rock bolting, slope retention systems, shotcrete, altering slope geometry, dewatering the slope, and revegetation. Several researchers (Ritchie 1963; Pierson et al. 1990; Pantelidis 2009 and Bar et al. 2016) have outlined some guidelines for designing passive measures.

It is suggested to construct a protection dam on the slope. It is built from locally available stones suitable for the natural texture of the region. Fig. 32 illustrates the optimum location of the dam with specifications of a width of 1.5 m, a height of 2 m, a length of 15 m, and resilient to a total kinetic energy of 500 kJ. Although the jump heights on the slope profile would not reach significant levels (generally <50 cm), the size of in-situ blocks that can detach from the investigated ignimbrite rock is likely to be greater than 2 m when the discontinuity spacing values are considered in Table 1. For this reason, the height of the rock holding structure should be at least 2 m to prevent the block from passing over the wall along the long axis during the rolling (even if it does not bounce), as seen in Fig. 32.

4. Conclusions

This study investigated the possibility of rock falls to the buildings in a historical settlement area from a slope. According to the kinematical, finite element, and rockfall analyses, the following conclusions were driven from the study.

- As a result of the investigations and measurements conducted in the field, several discontinuity systems can create kinematically different rock mass instabilities in the said slope. Accordingly, there is a potential for wedge and block toppling type discontinuity-controlled instability in the examined slope.
- Wedge type shear failure shows the highest potential (16.63%), while block toppling has a possibility of 8.13%.

- In the FEM analysis, the overall stability of the slope was found as relatively high with SRF=2.19. This value indicates that it was impossible to observe a complete failure of the slope in a short period.
- For more accurate results, various sizes and shapes of blocks were examined in the 2D rockfall analysis. The results clearly showed that the detached ignimbrite blocks from the steep slope would not reach the houses on the downslope. However, necessary preventive measures should be implemented to cease any negative effects in the future.
- Accordingly, it was recommended to build a protection dam made of locally available stones suitable for natural texture, with specifications in 2 m high, 1.5 m wide, 15 m long, and resistant to 500 kJ total kinetic energy.
- It has been observed that the steel fence/net (rockfall barriers or catch fences), which is widely used in rockfall prevention projects, is not suitable for the studied rockfall danger area due to the gentle slope and the natural texture.
- The proposed dam is only for protecting the houses located in parcel no 509 from the danger of rockfall, but not for the other houses in the surroundings.

References

Agliardi F, Crosta G. (2003). High resolution three-dimensional numerical modelling of rockfalls. Int J Rock Mech Min Sci, 40:455–71.

Alejano, L. R., Gonzalez J., Muralha J. (2012). Comparison of different techniques of tilt testing and basic friction angle variability assessment. Rock Mech Rock Eng 45:1023–1035.

Alemdag, S., Zeybek, H. I., Kulekci, G. (2019). Stability evaluation of the Gümüşhane-Akçakale cave by numerical analysis method. Journal of Mountain Science, 16(9), 2150–2158.

Ansari, M.K., Ahmad, M., Singh, R., Singh, T.N. (2015). Correlation between Schmidt hardness and coefficient of restitution of rocks. Journal of African Earth Sciences, 104:1-5.

Asteriou, P., Saroglou, H., Tsiambaos, G. (2012). Geotechnical and kinematic parameters affecting the coefficients of restitution for rock fall analysis. Int J Rock Mech Min Sci, 54:103–113.

Attewell, P., Farmer, I. (1976). Principles of Engineering Geology. London.

Ayhan, A., Papak, İ. (1988). Aksaray-Taşpınar-Altınhisar-Çiftlik-Delihebil (Niğde) Civarının Jeolojisi, MTA Raporu (in Turkish).

Azami, A., Yacoub, T., Curran, J. H. 2012. Effects of strength anisotropy on the stability of slopes. In: GeoManitoba 2012.

Bar, N., Nicoll, S., Pothitos, F. (2016). Rock fall trajectory field testing, model simulations and considerations for steep slope design in hard rock. APSSIM.

Barton, N. R. (1973). Review of a new shear strength criterion for rock joints. Eng Geol 7, 287-332.

Barton, N. (1976). The shear strength of rock and rock joints. Int J Rock Mech Min Sci Geomech Abstr 13:255–279.

Barton, N.R., Choubey, V. (1977). The shear strength of rock joints in theory and practice. Rock Mech, 10:1-54.

Barton, N.R., Lien, R., Lunde, J. (1974). Engineering classification of rock masses for the design of tunnel support. Rock Mech 6(4):189–236.

Basson, FRP (2012). Rigid body dynamics for rockfall trajectory simulation. In: Proc. 46th US Rock Mech. & Geomech. Symp. 24–27 June 2012, ARMA, Chicago.

Beekman, P.H. (1966). Aksaray-Gelveri-Çınarlı Bölgesinin Jeoloji Raporu, MTA Raporu (in Turkish).

Bell, F.G. (2007). Engineering Geology, Butterworth-Heinemann, 2nd Ed., 581 p.

Bieniawski, Z.T. (1989). Engineering Rock Mass Classifications. John Wiley & Sons, New York.

Binal, A. (1996). Investigation of the instability mechanisms observed in volcano-sedimentary rocks at Aksaray-Ihlara valley. MSc thesis, Hacettepe University, Ankara (in Turkish).

Binal, A., Ercanoğlu, M. (2010). Assessment of rockfall potential in the Kula (Manisa, Turkey) Geopark Region. Environmental Earth Sciences, 61(7), 1361–1373.

Bozzolo, D., Pamini, R. (1986). Simulation of rock falls down a valley side. Acta Mechanica 63: 113-130.

Budetta, P., Santo, A. (1994). Morphostructural evolution and related kinematics of rockfalls in Campania (southern Italy): A case study, Eng. Geol 36, 197–210.

Chau, K.T., Wong, R. H. C., Wu, J. J. (2002). Coefficient of restitution and rotational motions of rockfall impacts. Int. J. Rock. Mech. Min. Sci; 39:69-77.

Dadashzadeh, N., Aras, C., Yesiloglu-Gultekin, N., Bilgin, A., Duzgun, H.S.B. (2014). Analysis of potential rockfalls and protection measures for the Mardin Castle, Turkey. Eurock 2014, ISRM European Regional Symposium, 1231-36.

Deere, D.U., Miller, R.P. (1966). Engineering classification and index properties for intact rocks. Tech Rep Air Force Weapons Lab, New Mexico, no AFNL-TR, 65–116.

Doğan, U., Koçyiğit, A., Yılmaz, E. (2019). Geomorphological evolutionary history of the Melendiz River Valley, Cappadocia, Turkey. Mediterranean Geoscience Reviews, 1(2):203-22.

Dorren, L.K.A. (2003). A review of rockfall mechanics and modelling approaches. Progress in Physical Geography, 27(1):69-87.

Dorren, L.K.A., Berger, F., Putters, US (2006). Real-size experiment sand 3-D simulation of rockfall on forested and non-forested slopes. Nat. Hazards. Earth Syst. Sci; 6:145-53.

Eberhardt, E., Stead, D., Coggan, J., Willenberg, H. (2002). An integrated numerical analysis approach to the Randa rockslide. In: Proceedings of the first European conference on landslides, Prague, pp. 355-62.

Evans, S.G., Hungr, O. (1993). The assessment of rockfall hazard at the base of talus slopes. Canadian Geotech J, 30:620-36.

Fu, W., Liao, Y. (2010). Non-linear shear strength reduction technique in slope stability calculation. Computers and Geotechnics, 37(3):288-98.

Giani, GP (1992). Rock Slope Stability Analysis. Rotterdam: Balkema.

Goodman, R. E. (1989). Introduction to Rock Mechanics, 2nd Edition. New York: John Wiley & Sons.

Hammah, R.E., Yacoub, T., Corkum, B., Curran, J.H. 2008. The practical modelling of discontinuous rock masses with finite element analysis. In: 42nd US Rock Mech Symp, pp. 56–63.

Hammah, R.E., Yacoub, T., Corkum, B., Wibowo, F., Curran, J.H. 2007. Analysis of blocky rock slopes with finite element shear strength reduction analysis. 1st Canada-U.S. Rock Mechanics Symposium, Vancouver, Canada, pp. 329-34.

Hammah, R.E, Yacoub, T., Curran, J. H. 2009. Variation of failure mechanisms of slopes in jointed rock masses with changing scale. 3rd CANUS Rock Mech Symp (Paper No. 3956), Toronto.Hoek, E., Bray, J. (1977). Rock Slope Engineering. 1st Edition, IMM, London.

Hoek, E. (2007). Practical Rock Engineering, 2007 Edition, Vancouver, Canada.

Hoek, E, Bray, J.W. 1991. Rock slope engineering. Elsevier Science Publishing, New York, p. 358.

Hoek, E., Carranza-Torres, C., Corkum, B. (2002). Hoek–Brown failure criterion—2002 edition. In: 1st North American rock mechanics symposium, Toronto, pp. 267-73.

ISRM (International Society For Rock Mechanıcs) (2007). The Complete ISRM Suggested Methods for Rock Characterization, Testing and Monitoring: 1974-2006. R. Ulusay, J.A. Hudson (editors), ISRM Turkish National Group, Ankara, Turkey, 628 p.

Kobayashi, Y., Harp, E.L., Kagawa, T. (1990). Simulation of rockfalls triggered by earthquakes. Rock Mech Rock Enginng 23:1-20.

Marinos, P., Hoek, E. (2000). GSI: a geologically friendly tool for rock mass strength estimation. Proc. Int. Conf. on Geotech. & Geol. Engingng, GeoEng2000, Technomic Publ., 1422-42, Melbourne.

Mas Ivars D. (2010) Bonded particle model for jointed rock mass. Ph.D. Thesis, KTH-Engineering Geology and Geophysics Research Group. Royal Institute of Technology (KTH)

Ozturk, H.S., Kocaman, S., Gokceoglu, C. (2019). A low-cost approach for determination of discontinuity orientation using smartphone images and application to a part of Ihlara Valley (Central Turkey). Engineering Geology, 254:63-75.

Pain, A., Kanungo, D.P., Sarkar, S. (2014). Rock slope stability assessment using finite element-based modelling – examples from the Indian Himalayas. Geomech Geoengng: An Int J, 9(3):215-30.

Pantelidis, L. (2009). Rock slope stability assessment through rock mass classification systems. Int. J. Rock. Mech. Min. Sci, 46(2):315-25.

Pierson, L.A., Davis, S.A., Van Vickie, R. (1990). The Rockfall Hazard Rating System Implementation Manual, Oregon State Highway Division, Salem, OR.

Ritchie, A.M. (1963). Evaluation of rockfall and its control: Highway Research Record. No. 17, Washington DC., pp. 13-28.

Robotham, M. E., Wang, H., Walton, G. (1995). Assessment of risk from rockfall from active and abandoned quarry slopes, IMM, Section A., 104: 25-33.

Rocscience Inc. (2020a). Dips Version 8.0 – graphical and statistical analysis of orientation data. https ://www.rocscience.com. Toronto, Ontario, Canada. Accessed 6 July 2020.

Rocscience Inc. (2020b). RocData Version 5.0 – rock and soil strength data analysis. https ://www.rocscience.com. Toronto, Ontario, Canada. Accessed 8 July 2020.

Rocscience Inc. (2020c). RS2 Version 2019 – finite element analysis for excavations and slopes. https ://www.rocscience.com. Toronto, Ontario, Canada. Accessed 8 July 2020.

Rocscience Inc. (2020d). RocFall Version 8.0 – statistical analysis of rockfalls. https ://www.rocscience.com. Toronto, Ontario, Canada. Accessed 10 July 2020.

Qian, Z. G. Li, A. J., Lyamin, A. V., Wang, C. C. (2017). Parametric studies of disturbed rock slope stability based on finite element limit analysis methods. Comp Geotech, 81:155–66.

Sarı, M., Çömlekçiler, F. (2007). Investigation of discontinuities observed in Kızılkaya ignimbrite and description of the rock mass. J. Fac. Eng. Arch. Selcuk Univ., 23(1–2), 207–216 (in Turkish).

Sari, M. (2009). The stochastic assessment of strength and deformability characteristics for a pyroclastic rock mass. Int J Rock Mech Min Sci, 46(3), 613–626.

Sari, M. (2019). Stability analysis of cut slopes using empirical, kinematical, numerical and limit equilibrium methods: the case of old Jeddah–Mecca road (Saudi Arabia). Environmental Earth Sciences, 78(21):621.

Sari, M. (2021). Secondary toppling failure analysis and optimal support design for ignimbrites in the Ihlara Valley (Cappadocia, Turkey) by finite element method (FEM). Geotech Geol Engng, https://doi.org/10.1007/s10706-021-01819-7

Sarikaya, M. A., Çiner, A., Zreda, M. (2015). Fairy chimney erosion rates on Cappadocia ignimbrites, Turkey: Insights from cosmogenic nuclides. Geomorphology, 234, 182–191.

Spadari, M., Giacomini, A., Buzzi, O., Fityus, S., Giani, G. P. (2012). In situ rockfall testing in New South Wales, Australia. Int J Rock Mech Min Sci, 49:84-93.

Stimpson, B. (1981). A suggested technique for determining the basic friction angle of rock surfaces using core. Int J Rock Mech Min Sci Geomech Abstr 18:63–65.

Şimşek, Ş. (1997). Ihlara (Kapadokya) Özel Çevre Koruma Bölgesinin Jeolojisi ve Bölgede Yer Alan Termal Kaynakların Hidrojeolojik ve Hidrokimyasal Araştırması ve Korumaya İlişkin Öneriler. Aksaray Valiliği, İl Kültür ve Turizm Müdürlüğü (in Turkish).

Taşpınar, M. (2015). Ihlara Vadisi (Aksaray) Boyunca Kaya Düşmelerinin Değerlendirilmesi. MSc Thesis, Aksaray University, 57 p. (in Turkish).

Tunusluoglu, M.C., Zorlu, K. (2009). Rockfall hazard assessment in a cultural and natural heritage (Ortahisar Castle, Cappadocia, Turkey). Environmental Geology, 56(5):963-72.

Ulusay, R. Sönmez, H. (2002). Kaya Kütlelerinin Mühendislik Özellikleri. TMMOB Jeoloji Mühendisleri Odası Yayınları, Ankara, 243 s.

UN Glossary (2020). United Nations Network on Public Administration-UNPAN, New York, USA. http://www.unpan.org/Directories/Glossary/. Accessed 15 August 2020.

Vick, L. M., Zimmer, V., White, C., Massey, C., Davies, T. (2019). Significance of substrate soil moisture content for rockfall hazard assessment. Natural Hazards and Earth System Sciences, 19(5):1105-17.

Wyllie, D.C., Mah, C.W. (2004). Rock slope engineering: civil and mining, 4th eds. Spon Press, New York.

Yan, P., Zhang, J., Kong, X., Fang, Q. (2020). Numerical simulation of rockfall trajectory with consideration of arbitrary shapes of falling rocks and terrain. Compt and Geotech, 122:103511.

Zorlu, K., Tunusluoglu, M.C., Gorum, T., Nefeslioglu, H.A., Yalcin, A., Turer, D., Gokceoglu, C. (2011). Landform effect on rockfall and hazard mapping in Cappadocia (Turkey). Environmental Earth Sciences, 62(8):1685-93

Figures

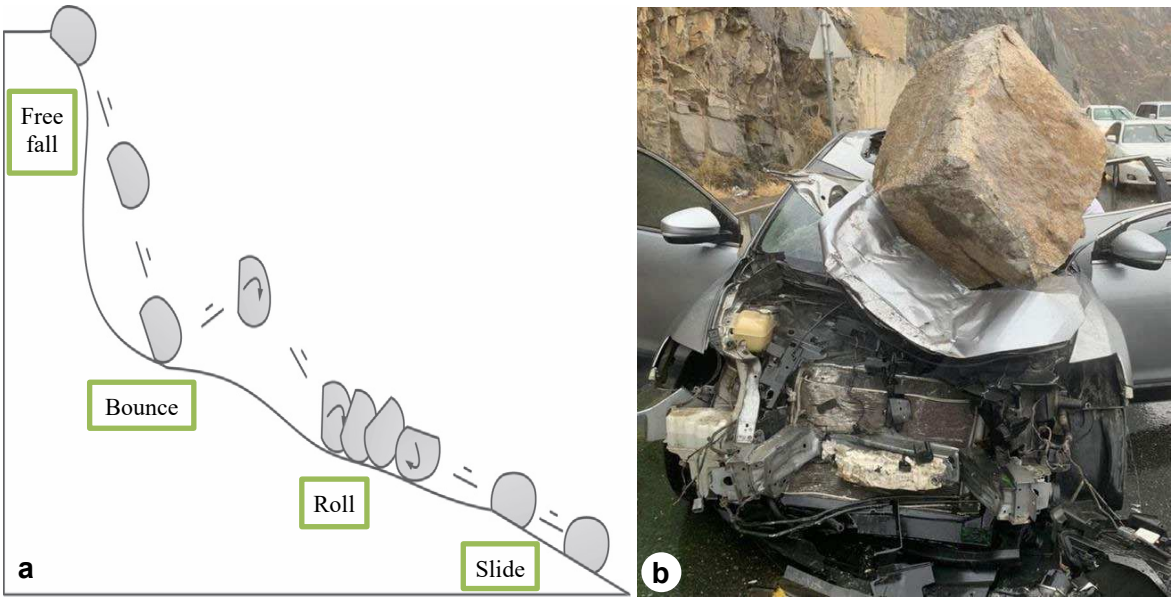

Fig. 1. a Four motion mechanisms of a typical rockfall (Yan et al. 2020), **b** A rockfall incident caused property damage at Al-Hada road, Saudi Arabia.

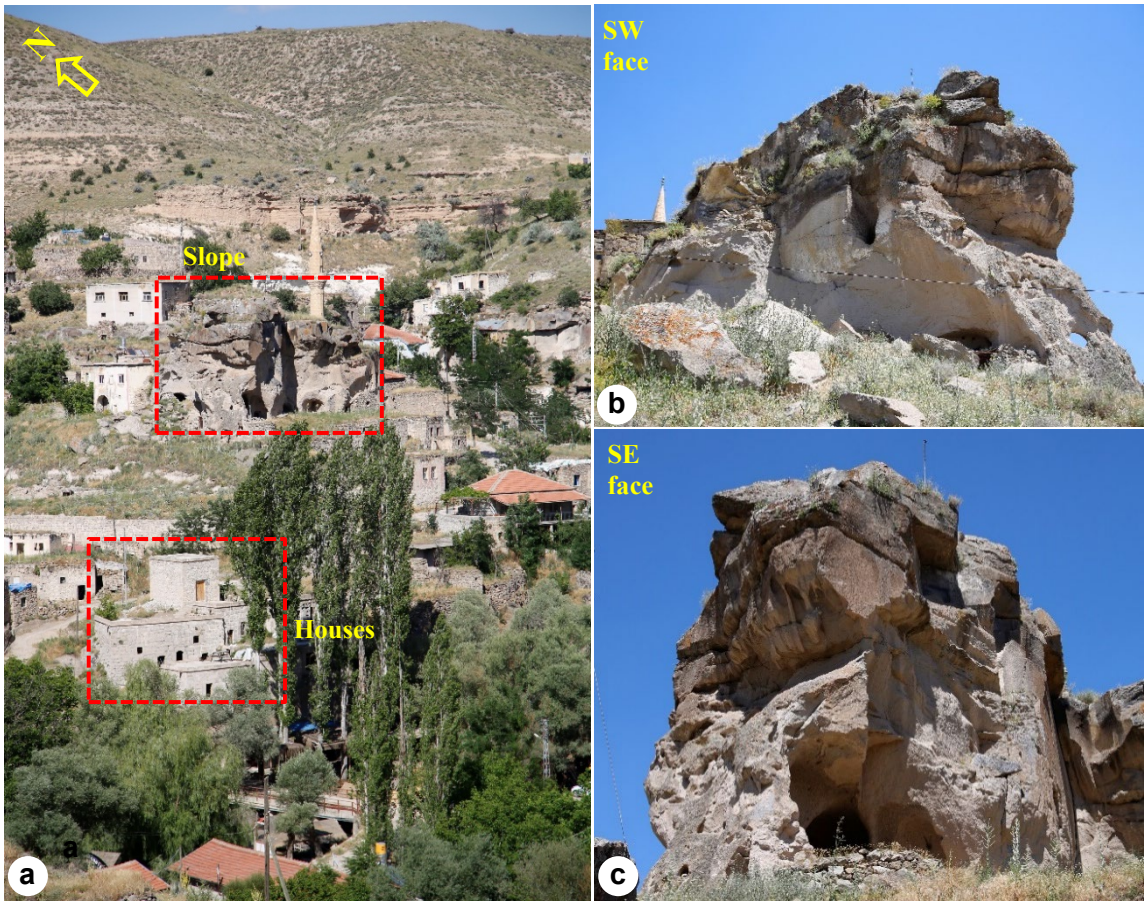

Fig. 2. a The slope and houses under rockfall danger, **b** SW face of the slope, **c** SE face of the slope.

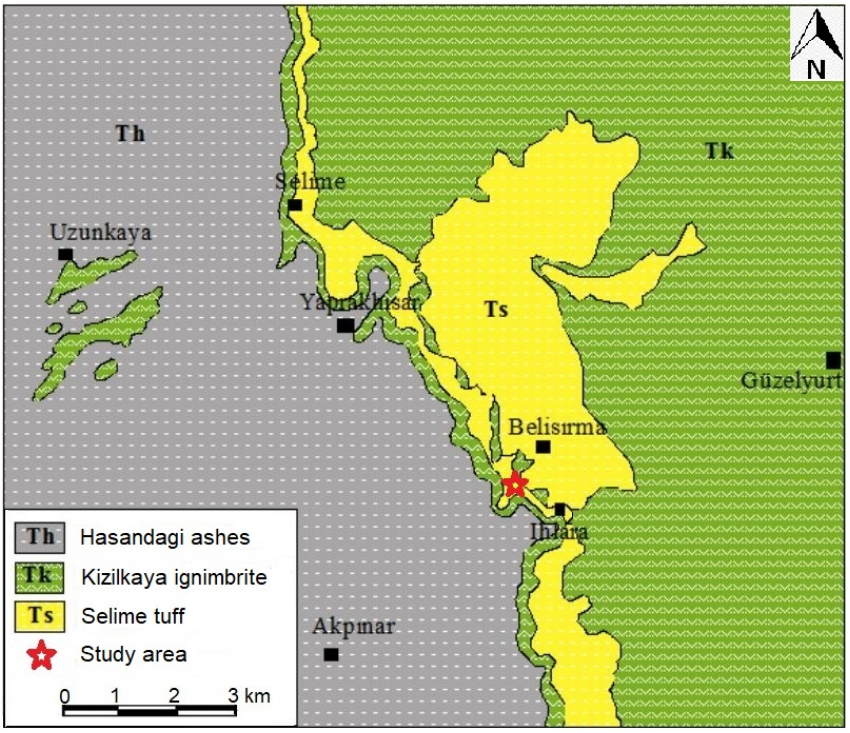

Fig. 3. Geological map of the study area (modified from Taşpınar 2015)

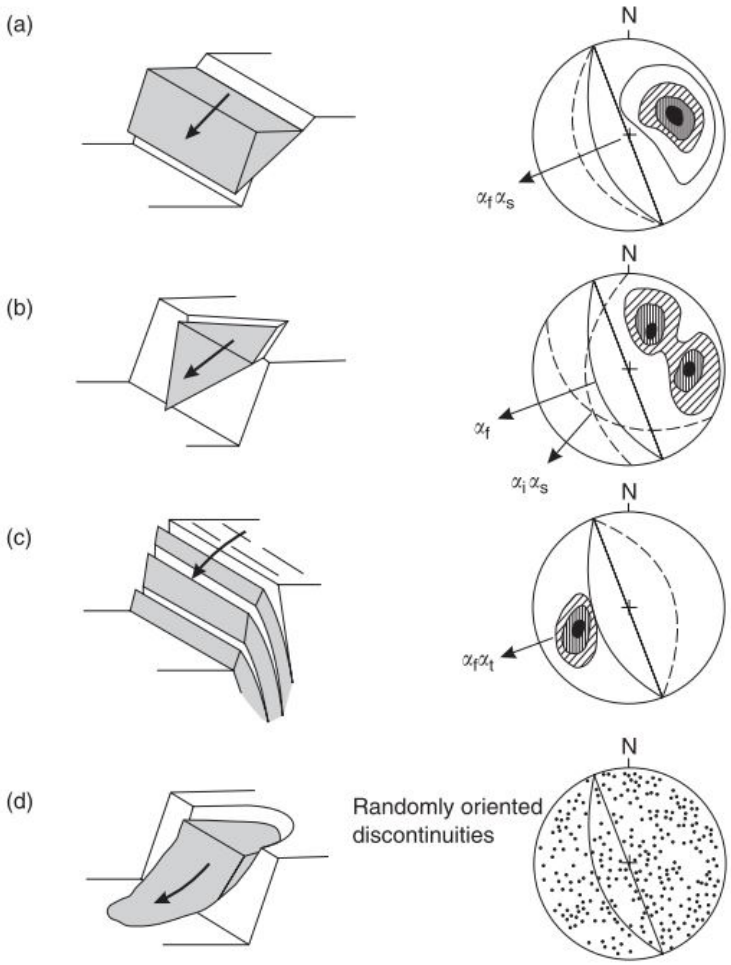

Fig. 4. Possible slope failure modes and conditions for the failure on the stereonet (Wyllie and Mah 2004), **a** Planar failure, **b** Wedge failure, **c** Toppling failure, and **d** Circular failure

Fig. 5. a Discontinuity orientation measurements in the field using Brunton compass, **b** Tilting test on rock blocks.

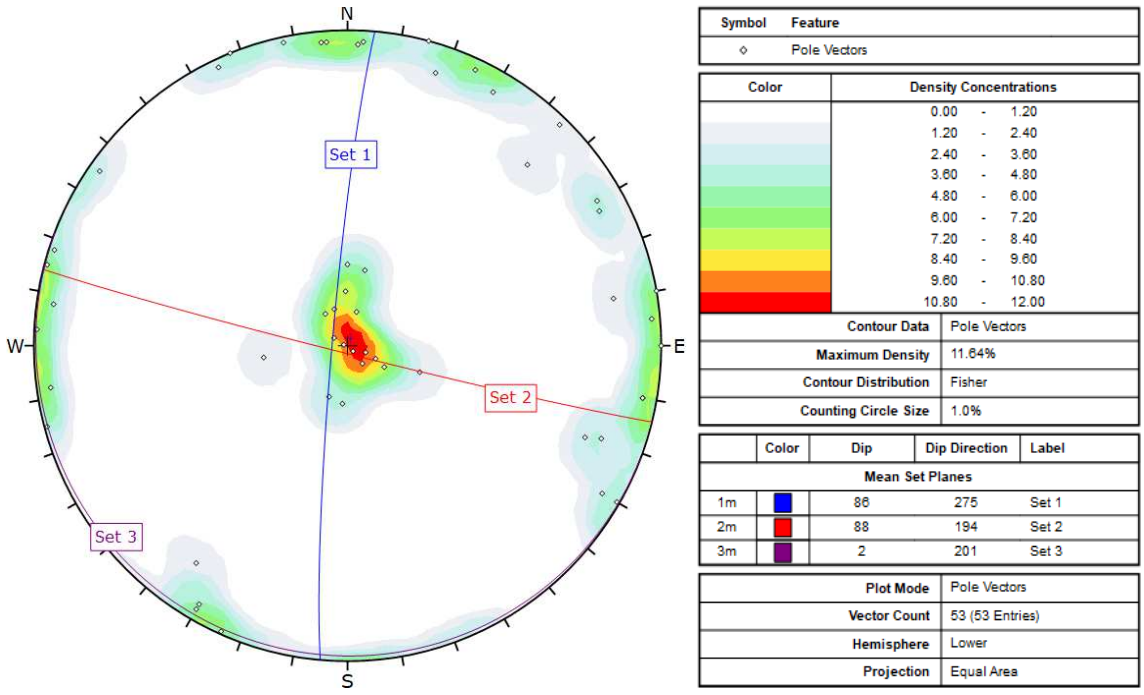

Symbol	Feature
◇	Pole Vectors

Color	Density Concentrations
	0.00 - 1.20
	1.20 - 2.40
	2.40 - 3.60
	3.60 - 4.80
	4.80 - 6.00
	6.00 - 7.20
	7.20 - 8.40
	8.40 - 9.60
	9.60 - 10.80
	10.80 - 12.00
Contour Data	Pole Vectors
Maximum Density	11.64%
Contour Distribution	Fisher
Counting Circle Size	1.0%

	Color	Dip	Dip Direction	Label
Mean Set Planes				
1m		86	275	Set 1
2m		88	194	Set 2
3m		2	201	Set 3

Plot Mode	Pole Vectors
Vector Count	53 (53 Entries)
Hemisphere	Lower
Projection	Equal Area

Fig. 6. Distribution of pole vector counters and defined major joint sets in the studied slope: Set 1:86/275, Set 2:88/194, Set 3:02/201

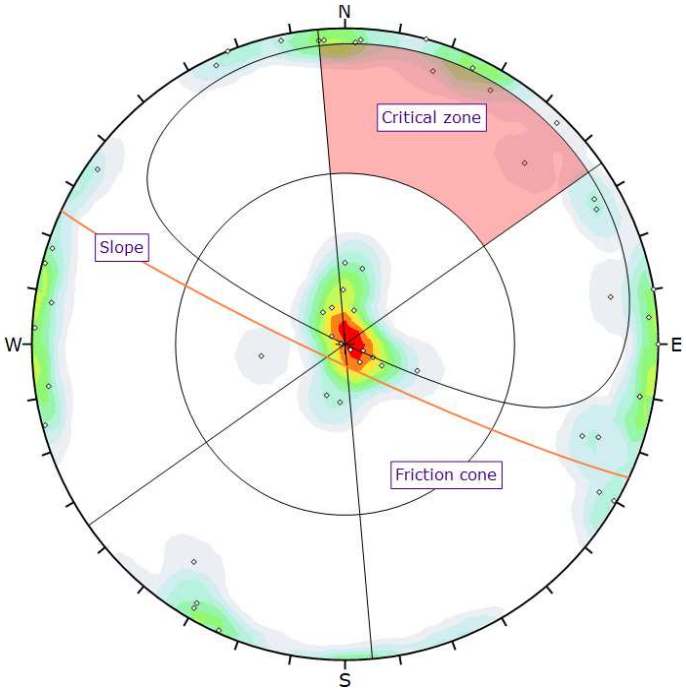

Symbol	Feature
◇	Pole Vectors

Color	Density Concentrations
	0.00 - 1.20
	1.20 - 2.40
	2.40 - 3.60
	3.60 - 4.80
	4.80 - 6.00
	6.00 - 7.20
	7.20 - 8.40
	8.40 - 9.60
	9.60 - 10.80
	10.80 - 12.00
Contour Data	Pole Vectors
Maximum Density	11.64%
Contour Distribution	Fisher
Counting Circle Size	1.0%

Kinematic Analysis	Planar Sliding
Slope Dip	85
Slope Dip Direction	205
Friction Angle	45°
Lateral Limits	30°

	Critical	Total	%
Planar Sliding (All)	3	53	5.66%
Planar Sliding (Set 2: Set 2)	3	17	17.65%

Plot Mode	Pole Vectors
Vector Count	53 (53 Entries)
Hemisphere	Lower
Projection	Equal Area

Fig. 7. Kinematical analysis of planar sliding in the studied slope

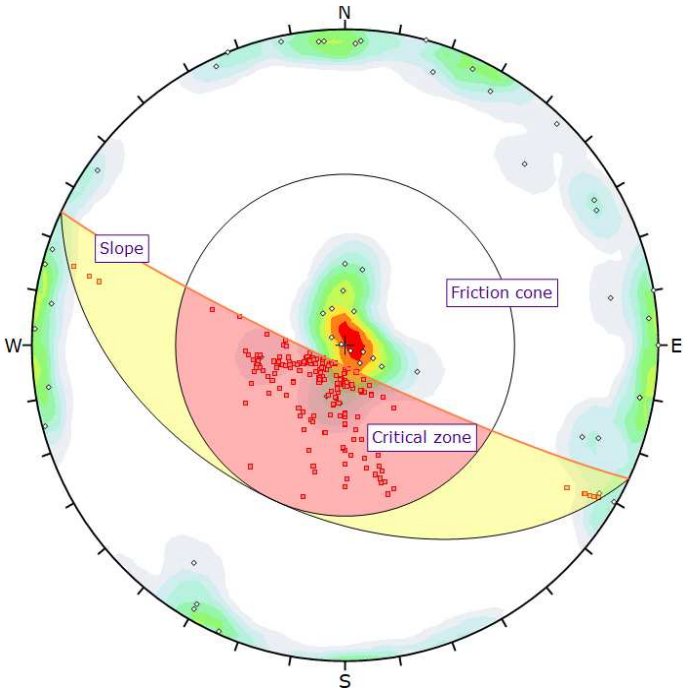

Symbol	Feature
◇	Pole Vectors
▫	Critical Intersection

Color	Density Concentrations
	0.00 - 1.20
	1.20 - 2.40
	2.40 - 3.60
	3.60 - 4.80
	4.80 - 6.00
	6.00 - 7.20
	7.20 - 8.40
	8.40 - 9.60
	9.60 - 10.80
	10.80 - 12.00

Contour Data	Pole Vectors
Maximum Density	11.64%
Contour Distribution	Fisher
Counting Circle Size	1.0%

Kinematic Analysis	Wedge Sliding
Slope Dip	85
Slope Dip Direction	205
Friction Angle	45°

	Critical	Total	%
Wedge Sliding	229	1377	16.63%

Plot Mode	Pole Vectors
Vector Count	53 (53 Entries)
Intersection Mode	Grid Data Planes
Intersections Count	1377
Hemisphere	Lower
Projection	Equal Area

Fig. 8. Kinematical analysis of wedge sliding in the studied slope

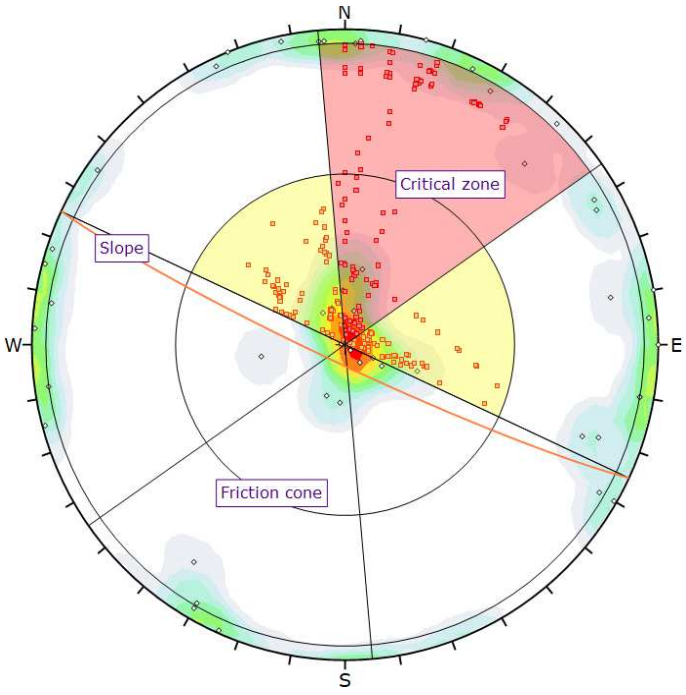

Symbol	Feature
◇	Pole Vectors
▫	Critical Intersection

Color	Density Concentrations
	0.00 - 1.20
	1.20 - 2.40
	2.40 - 3.60
	3.60 - 4.80
	4.80 - 6.00
	6.00 - 7.20
	7.20 - 8.40
	8.40 - 9.60
	9.60 - 10.80
	10.80 - 12.00

Contour Data	Pole Vectors
Maximum Density	11.64%
Contour Distribution	Fisher
Counting Circle Size	1.0%

Kinematic Analysis	Direct Toppling
Slope Dip	85
Slope Dip Direction	205
Friction Angle	45°
Lateral Limits	30°

	Critical	Total	%
Direct Toppling (Intersection)	112	1377	8.13%
Oblique Toppling (Intersection)	150	1377	10.89%
Base Plane (All)	14	53	26.42%
Base Plane (Set 2: Set 2)	4	17	23.53%
Base Plane (Set 3: Set 3)	10	17	58.82%

Plot Mode	Pole Vectors
Vector Count	53 (53 Entries)
Intersection Mode	Grid Data Planes
Intersections Count	1377
Hemisphere	Lower
Projection	Equal Area

Fig. 9. Kinematical analysis of block toppling in the studied slope

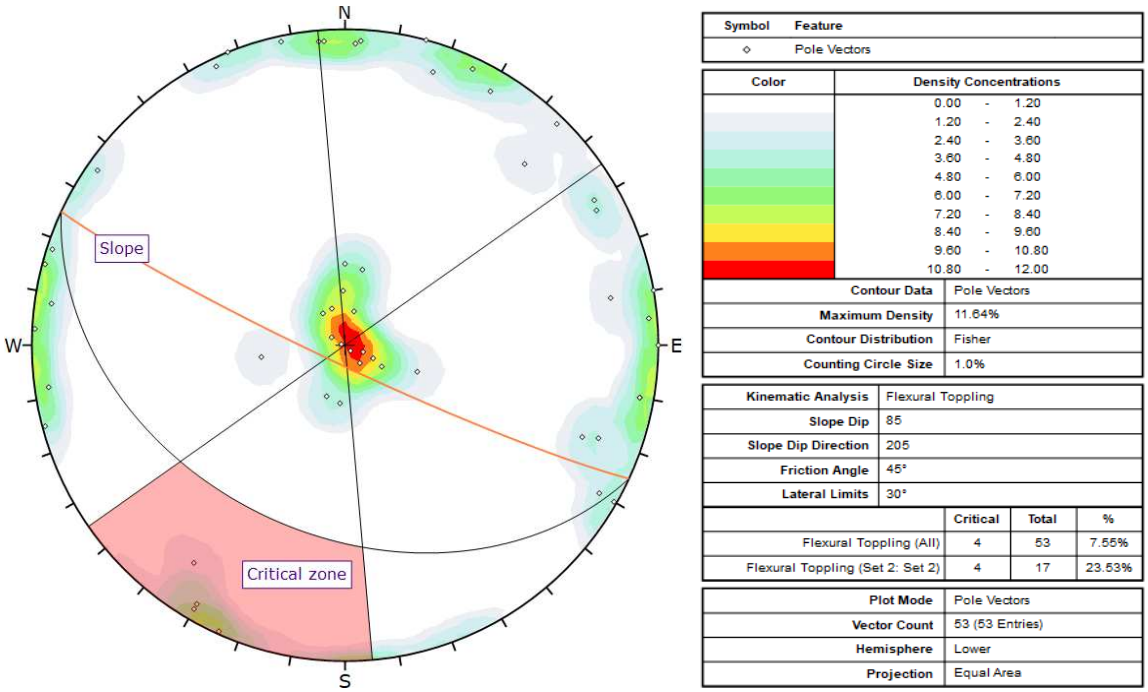

Symbol	Feature
◇	Pole Vectors

Color	Density Concentrations
	0.00 - 1.20
	1.20 - 2.40
	2.40 - 3.60
	3.60 - 4.80
	4.80 - 6.00
	6.00 - 7.20
	7.20 - 8.40
	8.40 - 9.60
	9.60 - 10.80
	10.80 - 12.00
Contour Data	Pole Vectors
Maximum Density	11.64%
Contour Distribution	Fisher
Counting Circle Size	1.0%

Kinematic Analysis	Flexural Toppling
Slope Dip	85
Slope Dip Direction	205
Friction Angle	45°
Lateral Limits	30°

	Critical	Total	%
Flexural Toppling (All)	4	53	7.55%
Flexural Toppling (Set 2: Set 2)	4	17	23.53%

Plot Mode	Pole Vectors
Vector Count	53 (53 Entries)
Hemisphere	Lower
Projection	Equal Area

Fig. 10. Kinematical analysis of flexural toppling in the studied slope

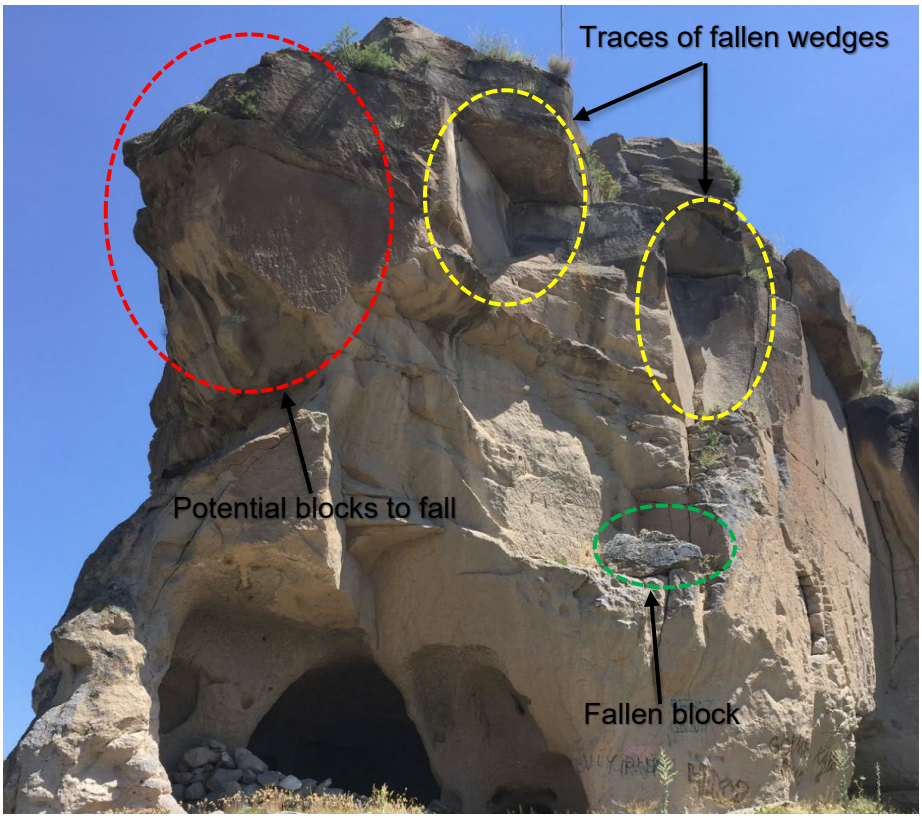

Fig. 11. Traces of fallen wedges on the SE face of the slope and potential blocks to fall.

Fig. 12. a Measurement of asperity amplitude and **b** Schmidt hardness value of rock surfaces in the field.

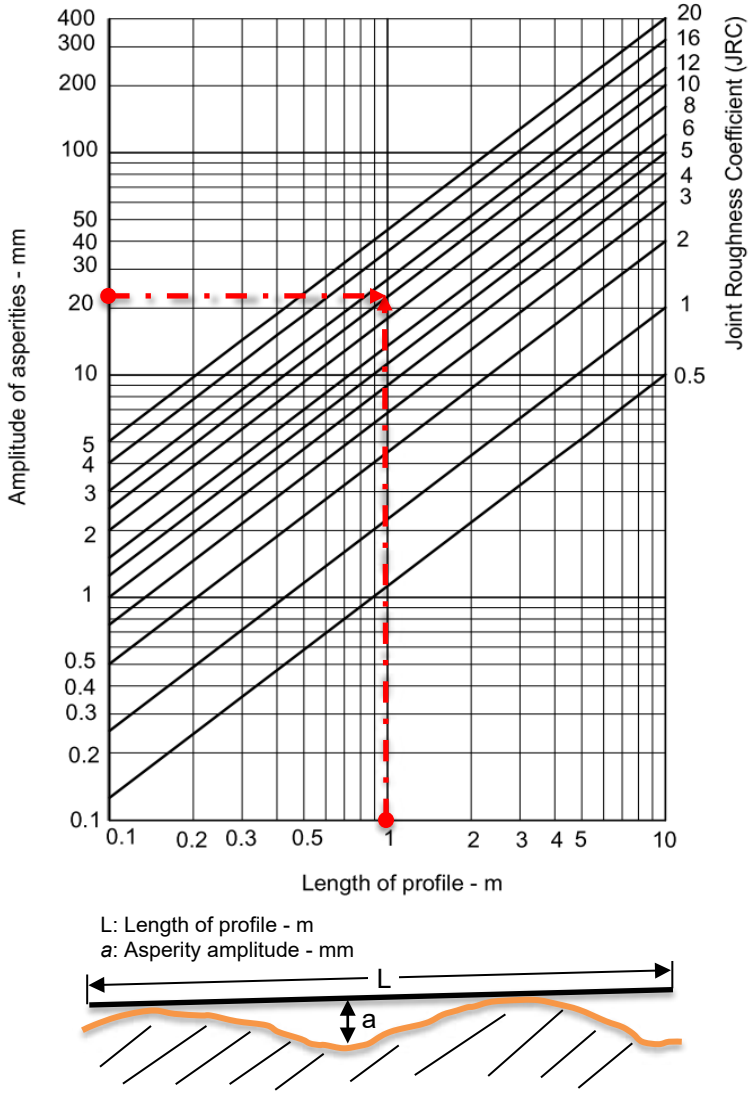

Fig. 13. Estimation of JRC based on the measurement of asperity amplitude along the length of a discontinuity surface profile.

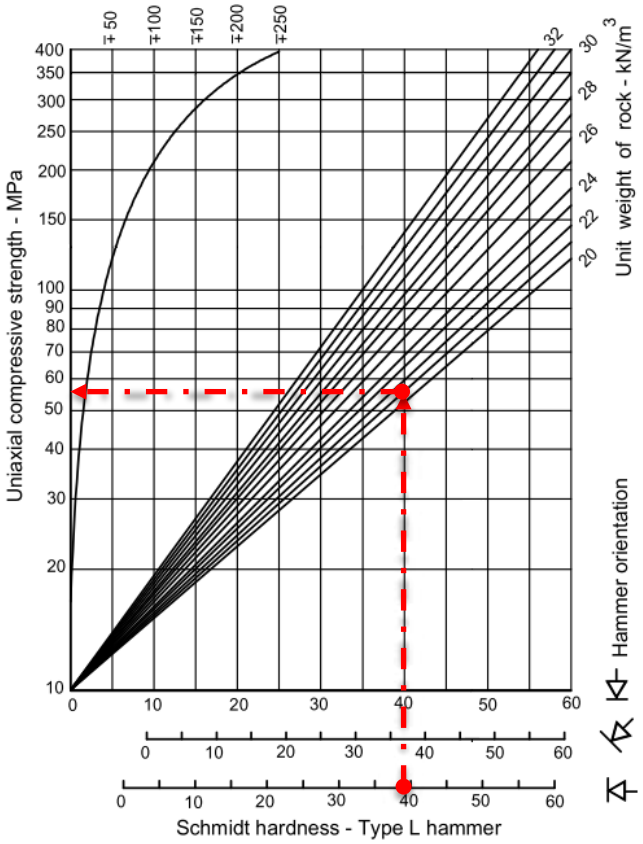

Fig. 14. Determination of JCS from the Schmidt rebound hardness value (Deere and Miller 1966).

Fig. 15. Application of the tilt test to Brazilian disc samples in the laboratory.

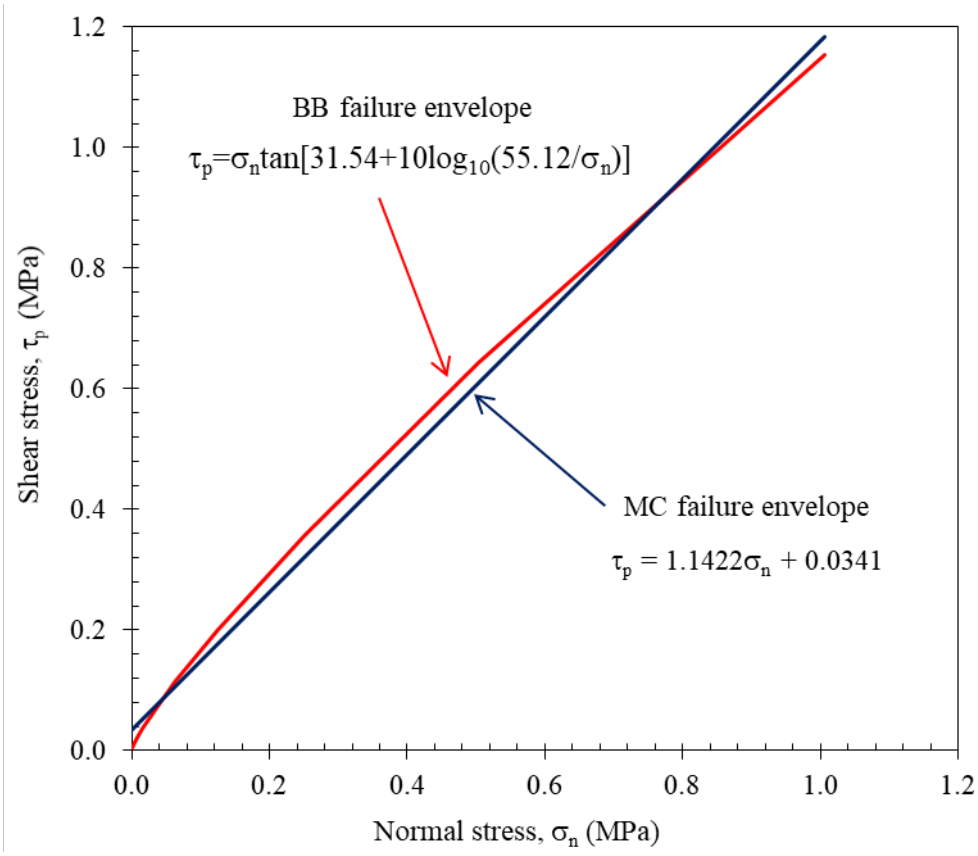

Fig. 16. Non-linear BB failure envelope and matching linear MC failure envelope for the joints.

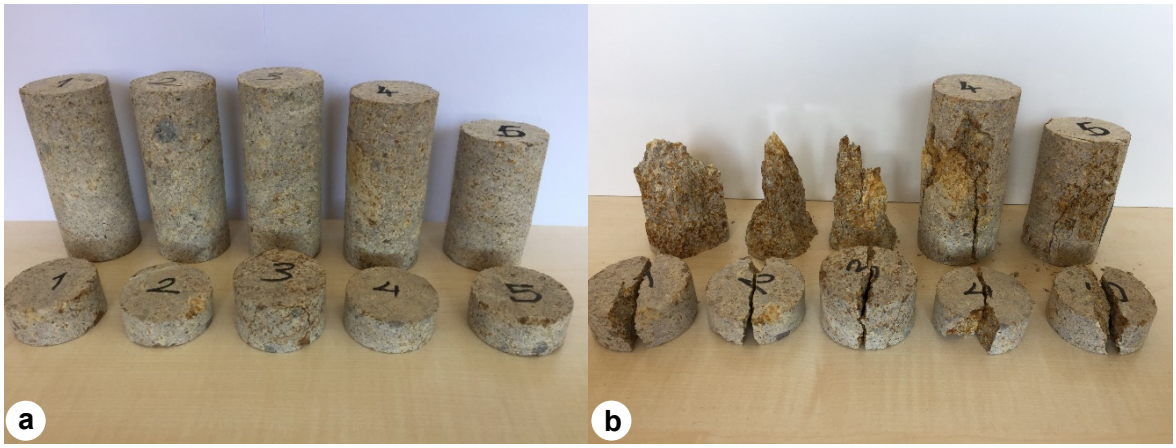

Fig. 17. a Prepared core samples for the UCS and BTS tests, **b** Samples after failure.

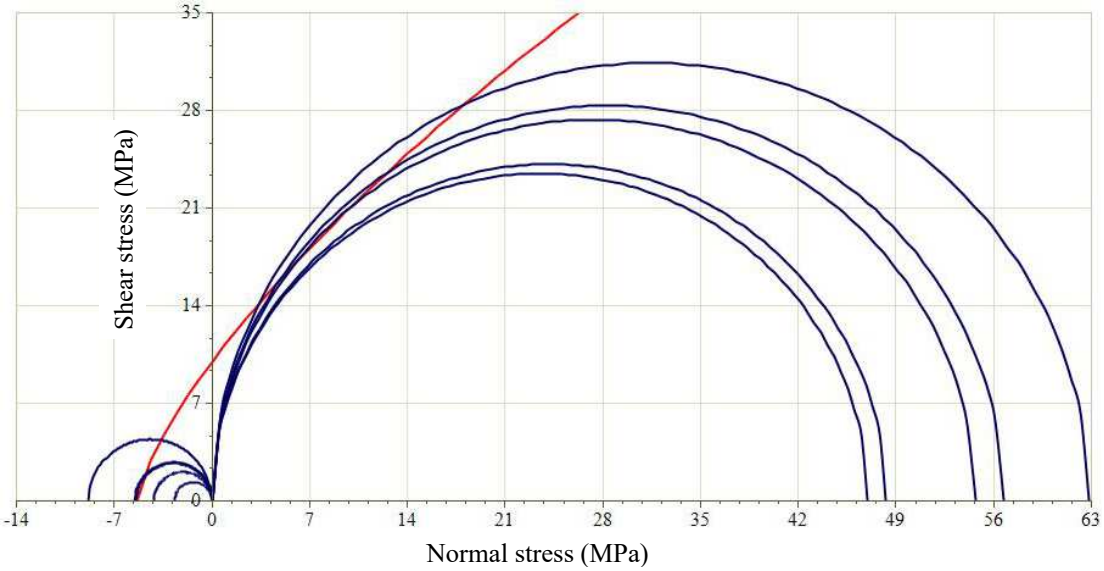

Fig. 18. HB failure envelope in normal-shear stress space for hard ignimbrite samples.

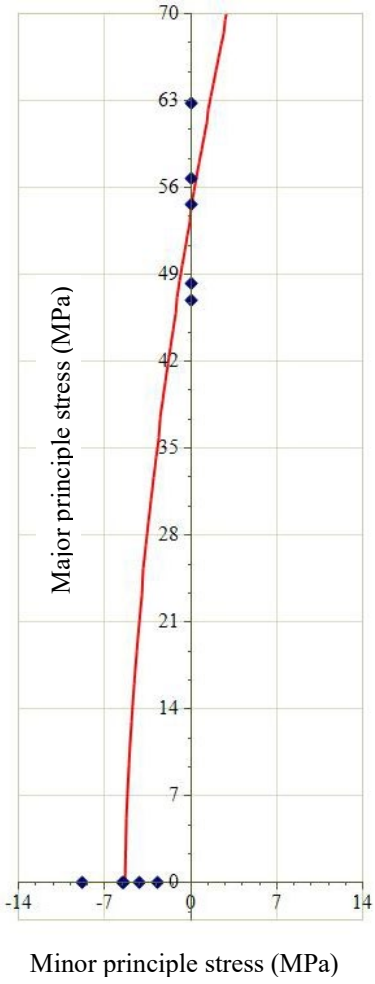

Fig. 19. HB failure envelope in principle stress space for hard ignimbrite samples.

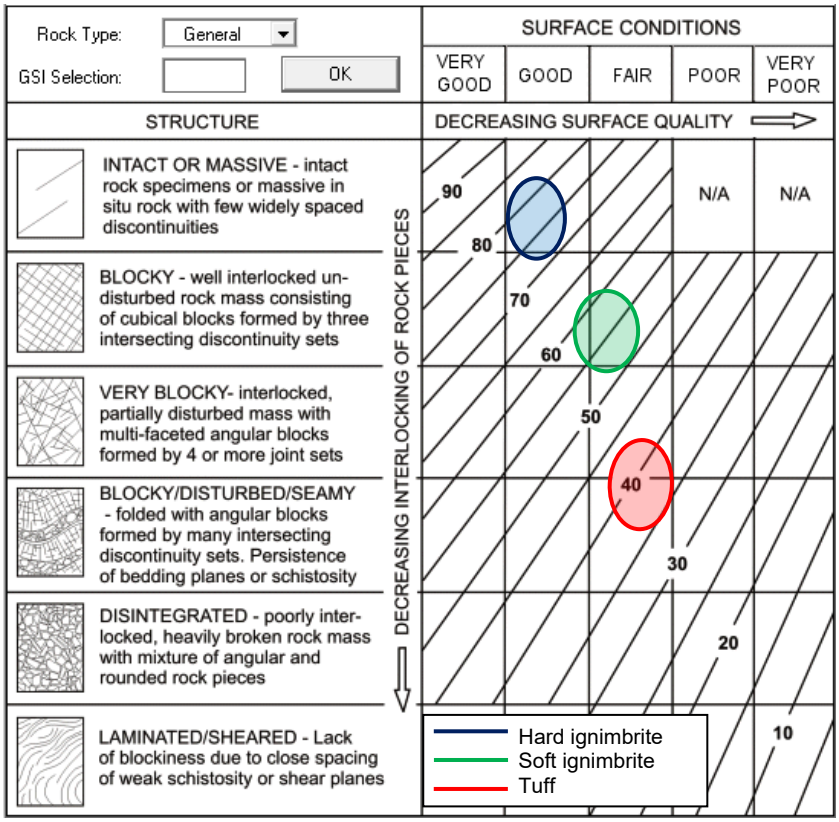

Fig. 20. Geological strength index chart and assigned GSI scores for the studied rock masses.

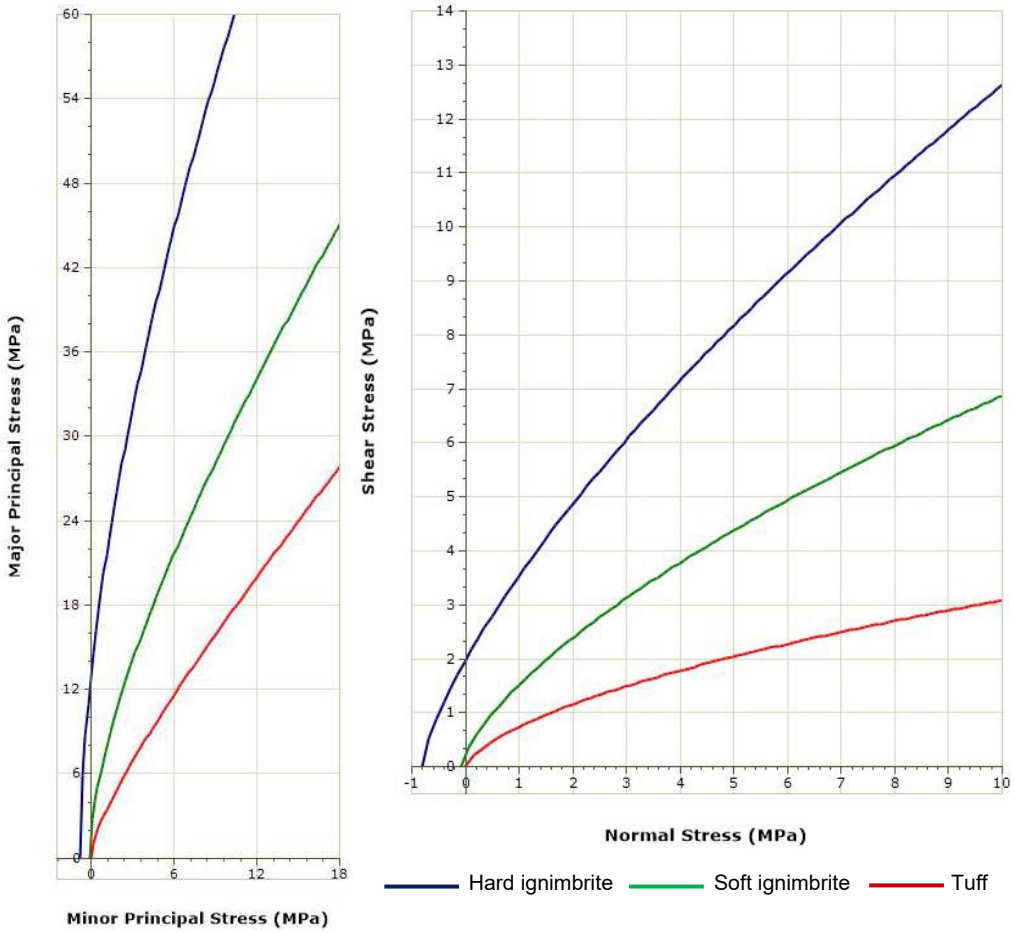

Fig. 21. HB strength envelopes for the rock masses; **a** In principal stress space, **b** Shear-normal stress space.

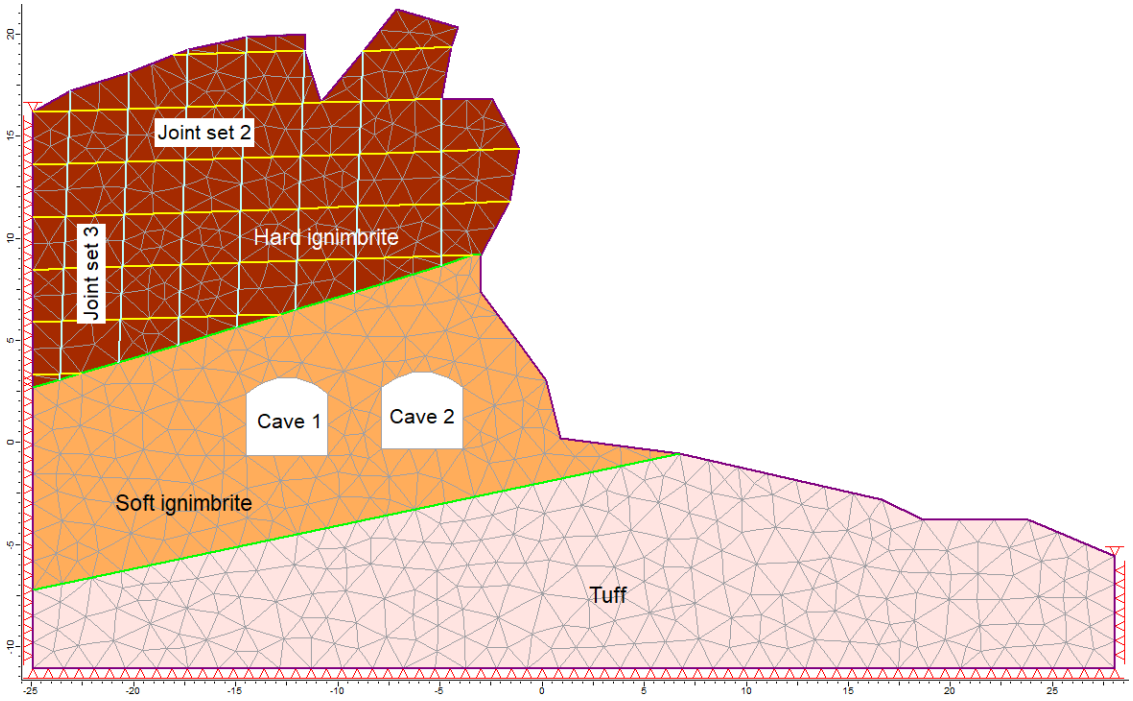

Fig. 22. The FEM model with specified dimensions of the studied slope case.

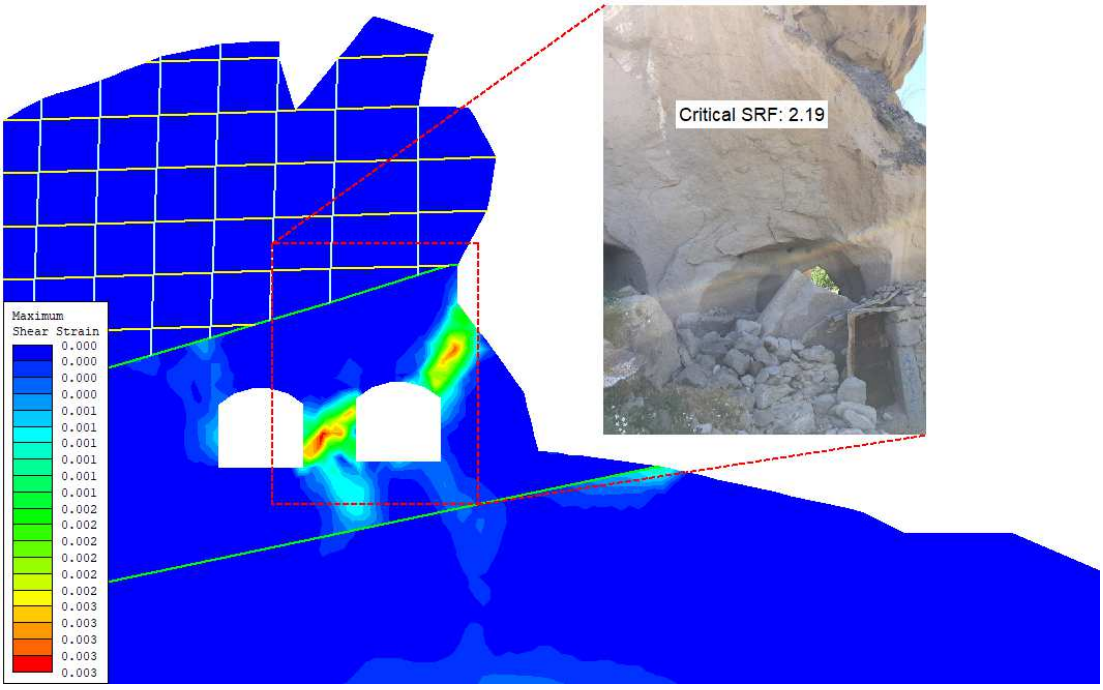

Fig. 23. Counters of the maximum shear strain on the FEM model and comparison of the exaggerated slope section with actual field condition.

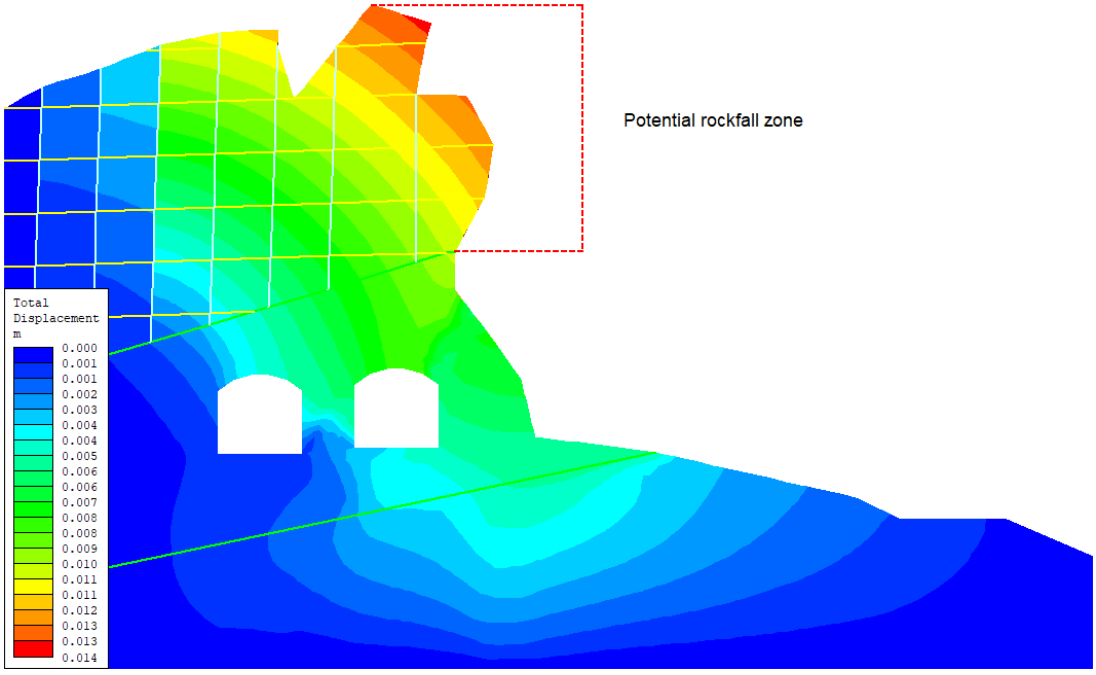

Fig. 24. Counters of the total displacement and potential rockfall zone on the FEM model of the slope.

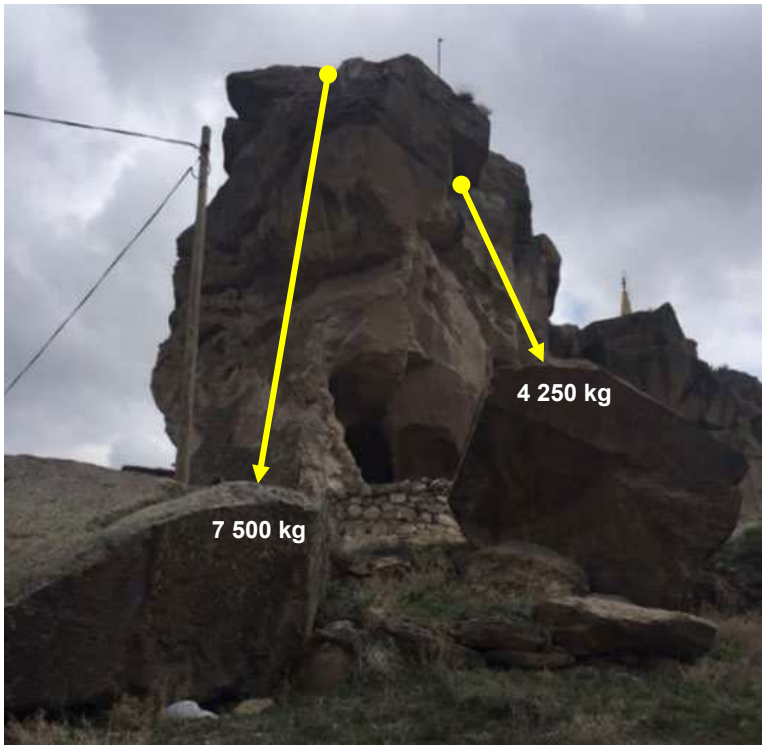

Fig. 25. Previously fallen blocks from the slope.

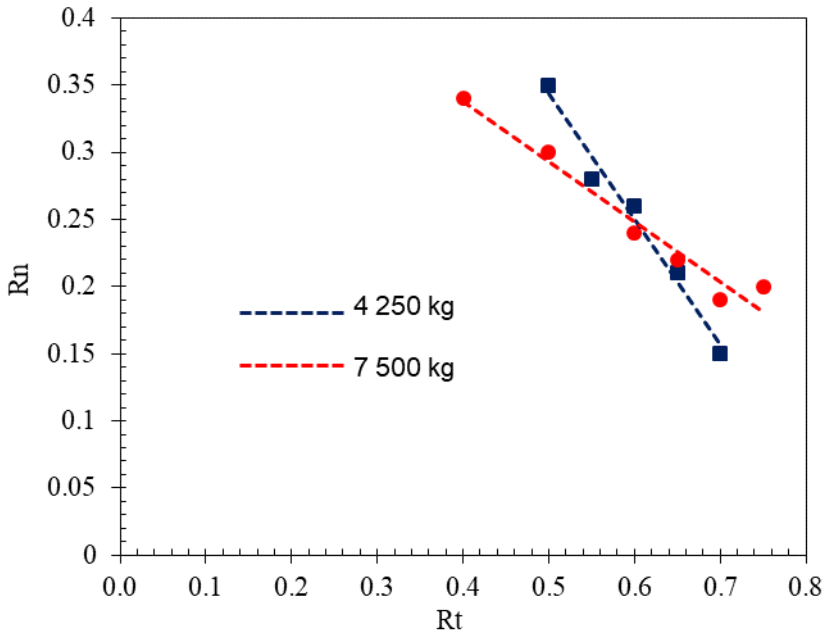

Fig. 26. Determination of normal and tangential restitution constants for the tuff in the study area.

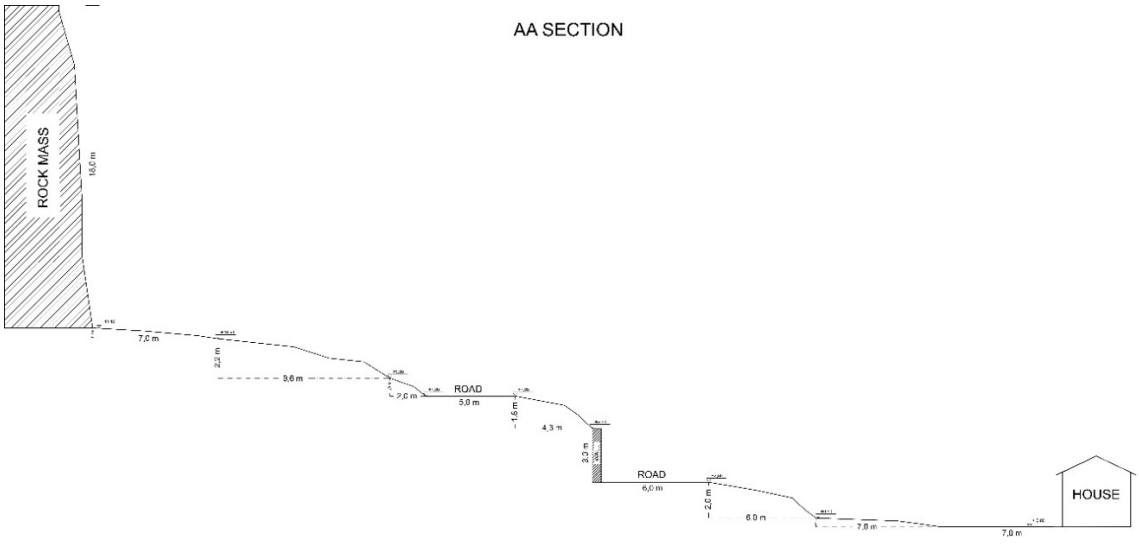

Fig. 27. AA-section profile used in the 2D rockfall program.

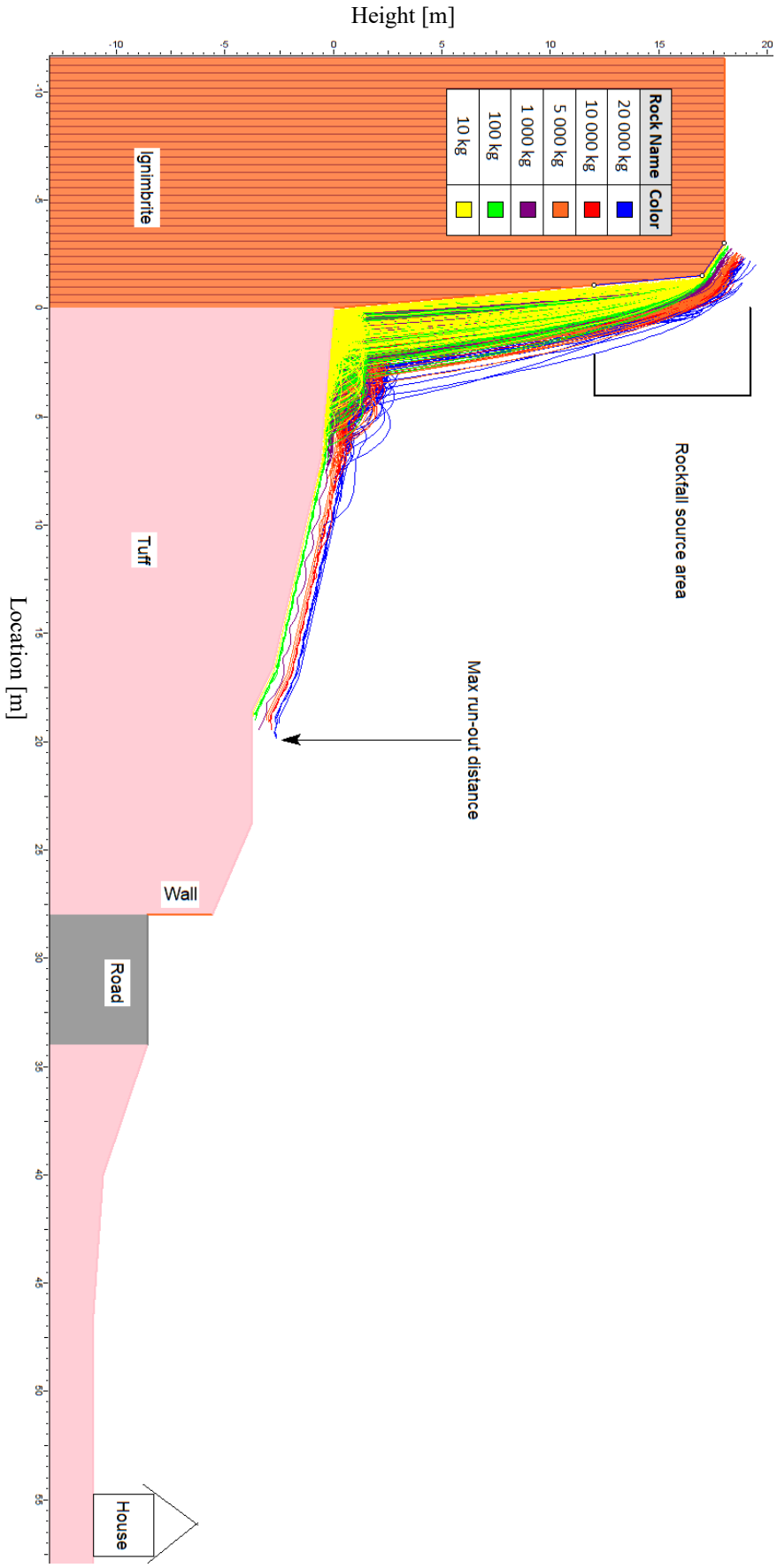

Fig. 28. Simulated rockfall trajectories along with the slope profile for different block types.

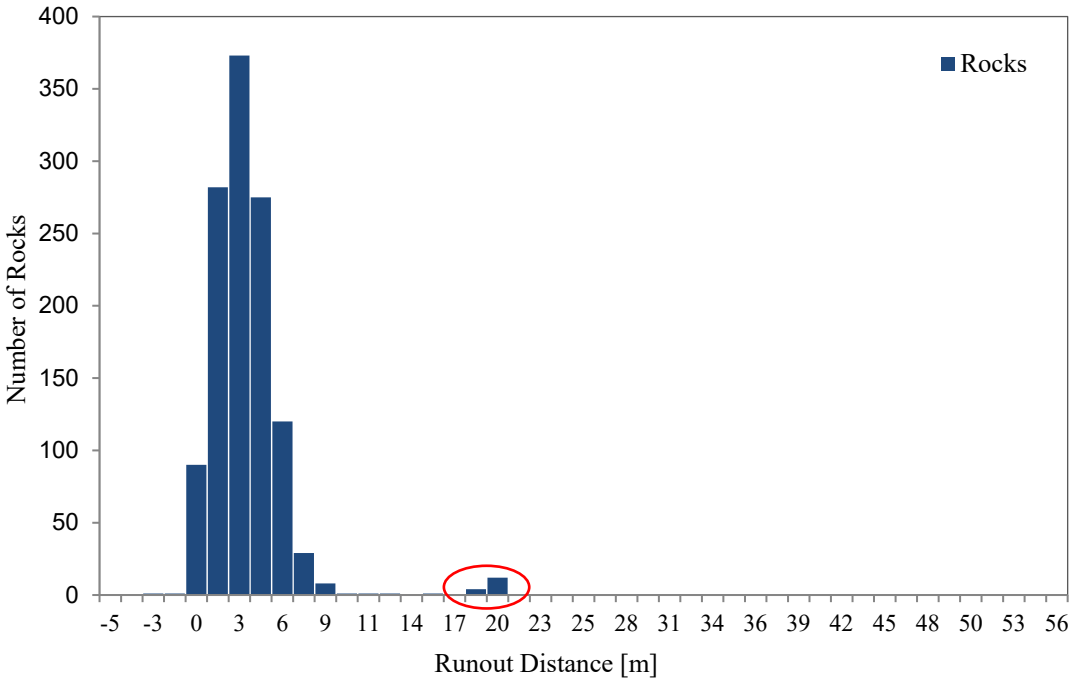

Fig. 29. Distribution of run-out distances of rock blocks along with the slope profile.

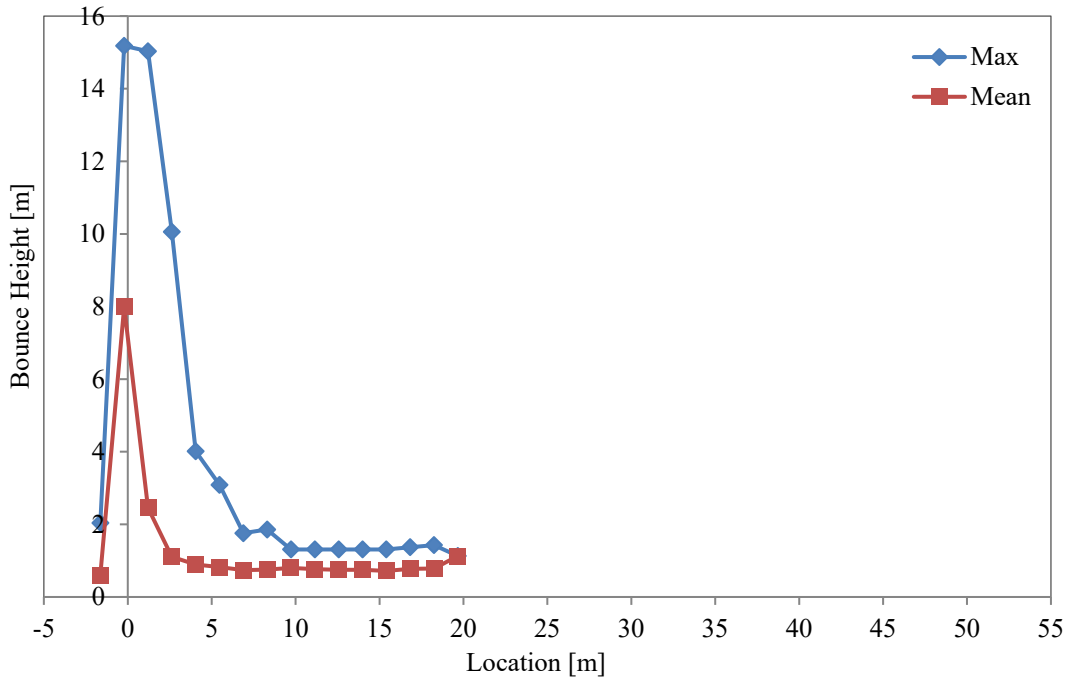

Fig. 30. Distribution of bounce height of rocks along with the slope profile.

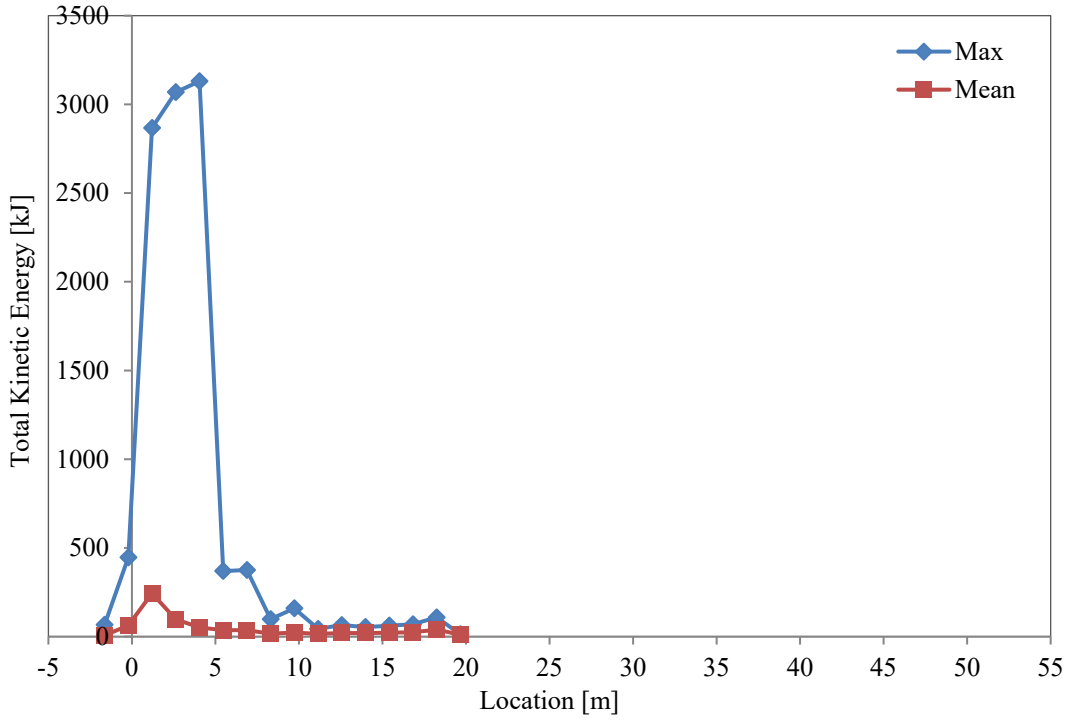

Fig. 31. Distribution of total kinetic energy of rocks along with the slope profile.

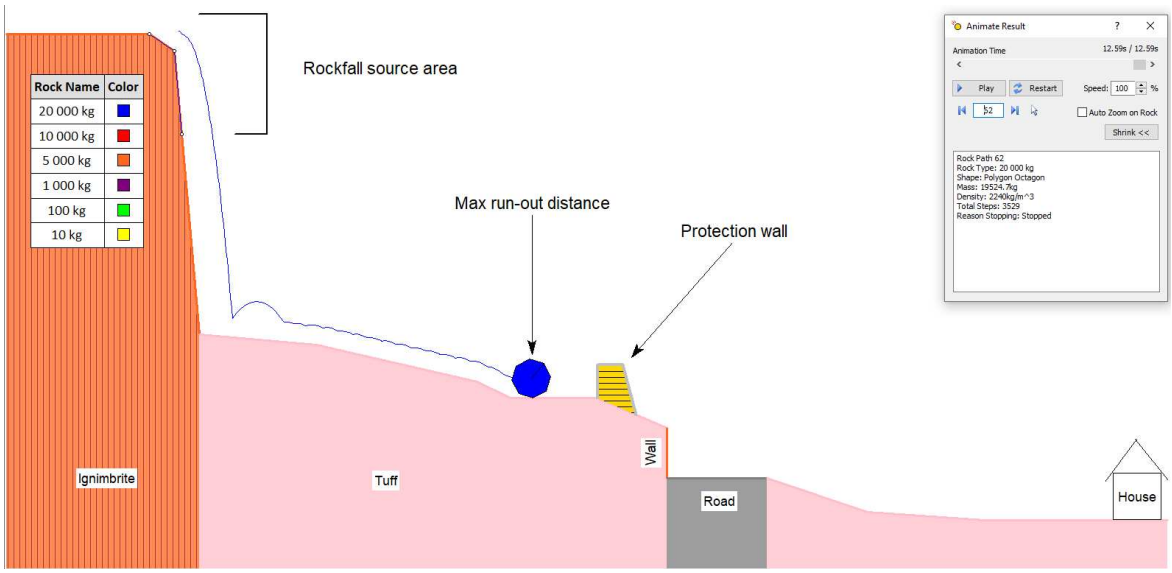

Fig. 32. Animation of a block of 20 tons dislodged from the slope and optimum location of the suggested protection dam.

Tables

Table 1. Properties of discountunity sets considered in kinematical analysis

Discontunity set no.	Discontunity orientation (dip/dip direction)	Slope orientation (dip/dip direction)	Discontunity friction angle (ϕ)	Discontunity spacing (m)	Discontunity aperture (cm)
Set 1	86º/275º			2.85	11.88
Set 2	88º/194º	85º/205º	45º	2.57	5.50
Set 3	2º/201º			1.44	2.33

Table 2. Kinematical analysis results

Failure type	Failure potential (%)	Critical set no.
Planar sliding	5.66	Set 2
Wedge sliding	16.63	Set 1, Set 2
Block toppling	8.13	Set 3
Flexural toppling	7.55	Set 2

Table 3. Rock material and rock mass parameters used in the FEM analysis

Input parameter	Hard ignimbrite	Soft ignimbrite	Tuff	Joint set 2	Joint set 3
γ_d (kN/m3)	21.75	19.75	17.52	-	-
UCS (MPa)	53.9	23.8	6.25	-	-
BTS (MPa)	5.33	2.42	0.58	-	-
c (MPa)	-	-	-	0.25	0.50
ϕ (º)	-	-	-	42	45
GSI (%)	75	55	38	-	-
m_i	10.0	8.5	7.2	-	-
E_t (GPa)	12.64	6.25	2.78	-	-

γ_d dry unit weight, UCS uniaxial compressive strength, BTS Brazilian tensile strength, c cohesion, ϕ friction angle, GSI geological strength index, m_i HB material constant, E_t Young's elastic modulus.

Table 4. Input parameters used in 2D rockfall program

Input parameter		Value
Engine type		Rigid body impact model
Number of throws		1,200 (200 per block type)
Block weight (kg)		10; 100; 1,000; 5,000; 10,000; 20,000
Block shapes		Various (sphere, square, triangle, egg, oval, ellipse, rhombus, rectangle, pentagon, hexagon and octagon)
Initial velocity (m/s)		0.5
Slope roughness		2
Sampling interval		50
Dynamic friction coefficient	Ignimbrite	0.45
	Tuff	0.30
	Stabilized road	0.50
Normal restutition coefficient (R_n)	Ignimbrite	0.35
	Tuff	0.25
	Stabilized road	0.40
Tangent restutition coefficient (Rt)	Ignimbrite	0.85
	Tuff	0.60
	Stabilized road	0.90

Table 5. Summary of the model run results

Parameter	Max	Mean	95%
Run-out Distance (m)	21.13	4.42	8.60
Bounce Height (m)	17.29	8.7	15.95
Total Kinetic Energy (kJ)	2023	430.3	2023
Translational Kinetic Energy (kJ)	2023	427.6	2023
Rotational Kinetic Energy (kJ)	42.88	14.71	42.88
Translational Kinetic Velocity (m/s)	16.78	10.53	16.78
Rotational Kinetic Velocity (rad/s)	27.43	6.51	27.43